

Probing T Tauri Accretion and Outflow with 1 Micron Spectroscopy

Suzan Edwards ^{1,3,4}, William Fischer ², Lynne Hillenbrand ^{3,5}, John Kwan ²

ABSTRACT

In a high dispersion 1 μm survey of 39 classical T Tauri stars veiling is detected in 80%, and He I $\lambda 10830$ and $P\gamma$ line emission in 97% of the stars. On average, the 1 μm veiling exceeds the level expected from previously identified sources of excess emission, suggesting the presence of an additional contributor to accretion luminosity in the star-disk interface region. Strengths of both lines correlate with veiling, and at $P\gamma$ there is a systematic progression in profile morphology with veiling. He I $\lambda 10830$ has an unprecedented sensitivity to inner winds, showing blueshifted absorption below the continuum in 71% of the CTTS compared to 0% at $P\gamma$. This line is also sensitive to magnetospheric accretion flows, with redshifted absorption below the continuum found in 47% of the CTTS compared to 24% at $P\gamma$.

The blueshifted absorption at He I $\lambda 10830$ shows considerable diversity in its breadth and penetration depth into the continuum, indicating that a range of inner wind conditions exist in accreting stars. We interpret the broadest and deepest blue absorptions as formed from scattering of the 1 μm continuum by outflowing gas whose full acceleration region envelopes the star, suggesting radial outflow from the star. In contrast, narrow blue absorption with a range of radial velocities more likely arises via scattering of the 1 μm continuum by a wind emerging from the inner disk. Both stellar and disk winds are accretion powered since neither is seen in non-accreting WTTS and among the CTTS helium strength correlates with veiling.

¹Five College Astronomy, Smith College, Northampton, MA 10163, sedwards@smith.edu

²Five College Astronomy, University of Massachusetts, Amherst, MA, 01003, kwan@astro.umass.edu, wfischer@astro.umass.edu

³Visiting Astronomer, Keck Observatory

⁴Guest Observer, Gemini/Keck-NIRSPEC program

⁵Dept. of Astronomy, California Institute of Technology, Pasadena, CA 91125, lah@astro.caltech.edu

Subject headings: stars: formation, winds, outflows, protoplanetary disks, pre-main-sequence

1. INTRODUCTION

In the formation of a star and its attendant planetary system the phase of disk accretion is always accompanied by mass outflow. Outflow collimation perpendicular to the disk plane and correlations between disk accretion rate and wind mass loss rate, with a rough proportion of $\dot{M}_w/\dot{M}_{acc} \sim 0.1$, certify the intimate relation between these two phenomena (Richer et al. 2000; Cabrit et al. 1990). Although the coupling of accretion and outflow is well documented, the means of launching the outflow remains unknown and is one of the major unsolved mysteries of star formation. There is a strong motivation to understand where and how energetic winds originate in accretion disk systems since they are strong contenders for a major role in mass and angular momentum transport in the disk (Ferreira & Casse 2004), for stellar spin-down (Königl 1991; Shu et al. 1994; Matt & Pudritz 2005), for heating the disk atmosphere (Glassgold et al. 2004), for hastening disk dissipation (Hollenbach et al. 2000), and for disrupting infalling material from the collapsing molecular cloud core (Terebey et al. 1984).

Most outflow models tap magneto-centrifugal ejection as the heart of the launching mechanism, where rotating fields in the disk fling material along inclined field lines and transport angular momentum away from the disk. A distinguishing characteristic among disk wind models is the location in the system where mass loading onto field lines occurs – either from the inner disk over a range of radii (Königl & Pudritz 2000) or from the radius at which the stellar magnetosphere truncates the disk, lifting most of the accreting material toward the star into magnetic funnel flows and ejecting the rest along opened stellar field lines emerging from this point (Shu et al. 1994). Others have explored the possibility that accretion-driven winds emerge via magnetohydrodynamic acceleration from the star rather than, or in addition to, the disk (Hirose et al. 1997; Kwan & Tademaru 1988; Matt & Pudritz 2005; Romanova et al. 2005; von Rekowski & Brandenburg 2006). Establishing the launch region for accretion powered winds is thus of considerable interest, since this can discriminate among the various wind theories and elucidate how angular momentum is removed from the star-disk environment.

Knowledge of accretion driven winds comes primarily from spatially extended collimated atomic and molecular jets comprised of high velocity ($200 - 400 \text{ km s}^{-1}$) outflowing material undergoing internal shocks (Hartigan et al. 1995; Reipurth & Bally 2001; Hartigan et al. 2004). These tracers yield basic wind energetics and establish the fundamental connection

between \dot{M}_w and \dot{M}_{acc} but provide only indirect information on the wind launching region. An intriguing result comes from spectroscopy at high spatial resolution of T Tauri "micro jets" revealing velocity asymmetries that have been interpreted as coherent rotation of the jet as would be imparted from an MHD disk wind launched from moderate disk radii of 0.5-2 AU (Coffey et al. 2004). However, recent three- dimensional simulations of line profiles formed in precessing jets with variable ejection velocities demonstrate that these conditions can produce similar velocity gradients, thereby calling into question the implied support for magnetocentrifugal wind acceleration models (Cerqueira et al. 2006).

Direct probes of the launch region can, however, only be made via high resolution spectroscopy. Confoundingly, most spectral features from sub-AU regions have kinematic signatures deriving from rotation or accretion rather than outflow. Near infrared lines of CO and H_2O are modeled as arising from inner accretion disks in Keplerian rotation at radii from 0.1 to 2 AU, precisely the region where the rotating jets are predicted to arise (Najita et al. 2003; Carr et al. 2004). Although modeling these features requires turbulent broadening and warm disk chromospheres, their symmetry reveals no evidence for outflowing gas from the upper disk layers. A possible signature of a wind emerging from the disk over radii ranging to tens of AU, is seen in the 'low velocity component' (LVC) of cTTS forbidden lines, distinguished from the 'high velocity component' (HVC) by smaller blueshifts (~ 10 km s $^{-1}$), smaller spatial extensions, and line ratios indicative of formation under conditions of higher density, although its interpretation as the launch of an extended disk wind remains unconfirmed (Hartigan et al. 1995; Kwan & Tademaru 1995).

However, outflow velocities of 200 to 500 km s $^{-1}$ characteristic of jets and HVC forbidden line emission point to an origin deeper in the potential well of the accretion disk system – either the very inner disk, the star-disk interface, or the star itself. These regions, where the stellar magnetosphere controls the accretion flow onto the star, are probed via permitted atomic emission lines from the infrared through to the ultraviolet and include a wide range of ionization states. Their line profiles, typically with strong and broad emission sometimes accompanied by redshifted absorption below the continuum and/or narrow centered emission, are attributed to formation in magnetospheric funnel flows and accretion shocks on the stellar surface (Edwards et al. 1994; Muzerolle et al. 2001; Herczeg et al. 2002, 2005). Until recently the only clear evidence for inner winds was blueshifted absorption superposed on the broad emission lines of H α , Na D, Ca II H&K, and MgII h&k, signifying the presence of a high velocity wind close to the star (Calvet 1997; Ardila et al. 2002) but yielding little information on the nature or location of the wind launching region.

Somewhat surprisingly, robust diagnostics of the inner wind in accretion disk systems are turning out to be lines formed under conditions of high excitation – He I and possibly

also C III and O VI (Edwards et al. 2003; Dupree et al. 2005) – arising in regions where temperatures exceed 15,000 K. The first indication of inner winds from regions with high excitation came from a study of He I $\lambda 5876$ and $\lambda 6678$ in a sample of 31 accreting cTTS. (Beristain et al. 2001, hereafter BEK). The high excitation of the helium lines restricts line formation to a region either of high temperature or close proximity to a source of ionizing radiation. In spite of these restrictions, the helium emission lines were found to have a composite origin, including contributions from a wind, from the funnel flow, and from an accretion shock.

Confirmation that broad helium emission traces inner winds in accreting stars came from observations of another line in the He I triplet series, $\lambda 10830$, which is a far more sensitive diagnostic of outflowing gas. This line, immediately following $\lambda 5876$ in a recombination-cascade sequence, has a highly metastable lower level, setting up a favorable situation for tracing outflowing gas in absorption. An initial look at 6 high accretion rate stars (AS 353A, DG Tau, DL Tau, DR Tau, HL Tau and SVS 13) focused on examples of He I $\lambda 10830$ profiles with exceptionally strong P Cygni wind signatures (Edwards et al. 2003). More recently He I $\lambda 10830$ profiles for two additional cTTS (TW Hya and T Tau) were also shown to have P Cygni profiles (Dupree et al. 2005). Both of these studies concluded that the winds tracked by helium absorption likely arise as a wind expanding radially away from the star, tracing the wind through its full acceleration from rest to several hundred km s⁻¹.

In this manuscript we present results of a census of He I $\lambda 10830$ in 39 cTTS and 6 wTTS plus 3 Class I sources from spectra collected with Keck II’s NIRSPEC. We find that this line is exceptionally sensitive not only to winds but also to infalling gas. Our spectra also yield simultaneous P γ profiles and 1 μ m continuum excess (veiling), providing a good combination of features to probe the relation between inner winds and accretion in young low mass stars. The remainder of the paper is organized as follows: *Section 2*: observations and data reduction, including sample selection and a description of the determination of the excess continuum emission and residual emission profiles, *Section 3*: accretion diagnostics: P γ and 1 μ m veiling, *Section 4*: wind diagnostic: He I $\lambda 10830$ *Section 5*: Class I sources, *Section 6*: discussion of magnetospheric accretion contributions to P γ and He I $\lambda 10830$ and wind contributions to He I $\lambda 10830$, *Section 7*; origin of 1 μ m veiling, *Section 8*: conclusions.

2. OBSERVATIONS AND DATA REDUCTION

Near-infrared echelle spectra of 39 classical T Tauri stars (CTTS), 6 weak T Tauri stars (WTTS) and 3 Class I sources were acquired with NIRSPEC on Keck II (McLean et al. 1998), using the N1 filter (*Y* band) with wavelength coverage from 0.95 to 1.12 μ m at $R = 25,000$

($\Delta V = 12 \text{ km s}^{-1}$). The detector is a 1024 x 1024-pixel InSb chip, and the spectrograph slit was $0.43'' \times 12''$. Spectra were taken in nodded pairs in an ABBA pattern, with the target separated by $5''$ in each AB pair. Typical exposure times were 300 seconds, integrated in each case to acquire $S/N \sim 70\text{--}80$ in the reduced 1-D spectra. All objects were observed on a 3 night run in November 2002 by Hillenbrand and Edwards. Three of our program stars were also observed on 22 November 2001 for Edwards and A. Dupree by the Gemini-Keck queue observers T. Geballe and M. Takamiya (see Edwards et al. 2003). In 2002 spectra were acquired without the image de-rotator, due to equipment malfunction. Although this prevents study of spatially extended emission, as reported for DG Tau (Takami et al. 2002), it is not a problem for extraction of a spectrum from the central point source, where most of the line emission and all of the line absorption arises.

Spectra were processed in IRAF using a modified version of a script originally provided by M. Takamiya. Data reduction steps included spatial rectification of the 2D images, wavelength calibration with a Xe/Ar/Kr/Ne arc lamp spectrum, correction for telluric emission, telluric absorption, and instrumental fringing, and extraction to 1-D spectra using IRAF’s *apall* package. Telluric emission was removed by subtraction of each AB pair of images, yielding two sky-subtracted spectra which were then coadded after spatial rectification and wavelength calibration. Telluric absorption features were removed by dividing the rectified, extracted, co-added, wavelength-calibrated spectra by the spectrum of an early-type standard observed at a similar airmass.

Division by a telluric standard also corrected the sinusoidal fringing pattern characterized by a spacing of $\sim 1.5 \text{ \AA}$ (10 pixels) and an amplitude $\sim 3\%$ of the continuum) for the 2002 data, where there was a good alignment (≤ 0.7 pixels) of the fringing pattern between the target and telluric standard. For the few 2001 spectra taken under queue observing, the fringe pattern was misaligned between target and standard by 1.5 to 4.5 pixels (0.5 to 1.5 times the instrumental resolution). For these spectra we determined the amount of fringe shift in wavelength by cross-correlating the target and standard spectra in a region free of spectral features, and found that the telluric absorption features shared the same misalignment. Consequently, after shifting the standard by the requisite amount, division by the standard conveniently removed both contaminating features. A final problem occasionally arose for stars observed at high air mass, when weak residual telluric features in the vicinity of the He I $\lambda 10830$ and $P\gamma$ lines appeared in the reduced spectrum. These were readily removed from the residual profile by determining their strength relative to stronger telluric features in the rest of the spectral order.

Our telluric standards were of early spectral type (O7 to B9), providing a nearly featureless continua over most of the orders yielding a good definition of telluric features. However,

they have strong photospheric lines of He I $\lambda 10830$ and $P\gamma$, our two primary spectral diagnostics. We thus took special care to define and remove these broad photospheric features in the standards so that spurious emission would not be induced in our T Tauri spectra. This was accomplished by first creating a synthetic spectrum of each standard where the observed profiles were modeled with a combination of Gaussian and Lorentzian functions, and then dividing the synthetic spectrum into the actual standard spectrum. We judged the fit effective when the final continuum-normalized spectra were flat in these spectral regions to within one percent. An additional correction for helium emission had to be made for HR 130 using a similar technique. The absence of any broad helium or hydrogen emission in our WTTS spectra (discussed in the following section) verifies that this procedure was effective. After removal of all of the above instrumental effects, the definition of the final spectrum is limited only by the signal to noise of the target and standard.

Although 13 echelle orders appear on the chip with the N1 filter, the first and last are severely contaminated by telluric absorption. Of the remaining eleven orders, the number and location of arc lamp lines is such that reliable wavelength solutions can be obtained for four full orders and five partial ones. The order extending from 1.081 to 1.096 μm contains both our prime spectroscopic diagnostics of He I $\lambda 10830$ and $P\gamma$ and also many photospheric features in late type stars. In addition to this order we identified two additional orders with abundant photospheric lines that we used for redundant estimates of the continuum veiling and determination of the stellar velocity. One, immediately to the blue of our prime order, extends from 1.066 to 1.081 μm and has numerous photospheric features and minimal contamination from telluric absorption. A second, although its full extension is from 0.971 to 0.986 μm , only had sufficient arc line coverage for wavelength calibration from 0.971 to 0.979 μm . Even with only half the order usable we found it to be preferable to other orders because its strong photospheric features were still detectable when photospheric lines in the other orders were obscured by broad metallic emission features which were sometimes found in stars with the highest continuum veiling.

2.1. Determination of Excess Continuum Emission and Residual Profiles

The 39 CTTS and 6 WTTS in our sample are identified in Table 1. All but two have spectral types from K0 to M5, with K7/M0 stars comprising the majority (27 stars). The remaining two are of solar type, SU Aur (G2) and GW Ori (G5). Most (30) are in the Tau-Auriga star formation complex, the rest are well studied T Tauri stars from associations including those in Orion and TW Hydra. The sample covers the full range of continuum emission excesses in the optical and ultraviolet found for CTTS and was selected to overlap

extensively with an earlier optical echelle survey of 31 CTTS appearing in Hartigan et al. 1995 (hereafter HEG) and Beristain et al. 2001 (hereafter BEK), thereby allowing a comparison of optical and infrared outflow and accretion diagnostics (including profiles of [O I] $\lambda 6300$, H α and He I $\lambda 5876$) for stars common to both studies. The current sample thus includes 30 of the 31 CTTS in HEG and BEK, identified in Table 1 by an entry for veiling at $\lambda 5700$ Å (r_V). Also included in Table 1 are disk accretion rates determined from veiling, spanning $\dot{M}_{acc} \sim 10^{-6}$ to $10^{-9} M_{\odot} yr^{-1}$, mass outflow rates from forbidden lines, spanning $\dot{M}_w \sim 10^{-7}$ to $10^{-10} M_{\odot} yr^{-1}$ and the corresponding ratio of \dot{M}_w/\dot{M}_{acc} .

We have determined both the $1 \mu m$ veiling r_Y , defined as the ratio of excess to photospheric flux in the Y band, and residual emission profiles at He I $\lambda 10830$ and $P\gamma$ for each of our objects. Our method for veiling determination follows Hartigan et al. (1989), matching an echelle order of an accreting star to that of a non-accreting standard of comparable spectral type to which has been added a constant continuum excess, i.e. the veiling, that reproduces the depth of the photospheric features in the accreting star. We used an interactive IDL routine kindly provided by Russel White to accomplish the requisite velocity shift of the standard via cross-correlation and the requisite rotational broadening of the standard before determining the required level of continuum excess. When a good match between the accreting star and the veiled standard is found, subtraction of the template yields a zero-intensity residual spectrum for the accreting star except in the vicinity of lines arising from accretion-related activity. Integrated equivalent widths for spectral lines were determined with an IDL routine kindly provided by Catrina Hamilton.

In Figure 1 continuum normalized spectra for each of the 6 WTTS (LkCa 4, TWA 3, TWA 14, V819 Tau, V826 Tau, and V827 Tau) are shown along with the CTTS GM Aur. Spectra in $\pm 500 \text{ km s}^{-1}$ windows are centered on the wavelength of the He I $\lambda 10830$ and $P\gamma$ lines, at rest with respect to the star as determined from the photospheric lines. In each region several photospheric features are marked with vertical lines in the upper spectrum of Figure 1 (GM Aur). In the He I $\lambda 10830$ region the 3 strongest photospheric features are Si I $\lambda 10830.1$, Na I $\lambda 10837.8$ and Si I $\lambda 10846.8$. In the $P\gamma$ region the 3 marked lines correspond to H I $\lambda 10941.1$ ($P\gamma$), Fe I $\lambda 10949.8$ and Mg I $\lambda 10956.3$. The remaining numerous absorption features in that region are part of a broad CN 0-0 band, not noise. V826 Tau is a spectroscopic binary (Mundt et al. 1983) and in our data the photospheric lines are double with a velocity separation of 21 km s^{-1} .

None of the 6 WTTS or GM Aur have any excess continuum emission ($r_Y < 0.05$), and only two of them have weak emission at He I $\lambda 10830$ or $P\gamma$ above an upper limit of $W_{\lambda} < 0.2$ Å. Both lines are weakly emitting in V826 Tau, with $W_{\lambda} = 0.8$ Å for helium and $W_{\lambda} \leq 0.3$ Å for $P\gamma$. TWA 14 has only helium in emission, with $W_{\lambda} = 0.6$ Å. The emission

equivalent widths for these 2 stars are several times weaker than the weakest emission found for the CTTS. Optical He I $\lambda 5876$ emission was also found to be rare among WTTS, seen in only 3 out of 10 WTTS by BEK, including V826 Tau. Both the optical and infrared helium emission may arise in an active chromosphere or a very weak accretion flow.

In earlier studies GM Aur has shown the hallmarks of an accreting CTTS – optical veiling, O I emission and strong H α (HEG, Gullbring et al. 1998). However, in our NIRSPEC data this is the only one of the 39 CTTS that shows no line emission in He I $\lambda 10830$ or P γ ($W_\lambda < 0.2 \text{ \AA}$), which we interpret as a sign that accretion has temporarily ceased. Its weak P γ absorption feature is similar in strength to that from the photosphere of an early K star (Hinkle et al. 1995). The spectral energy distribution for GM Aur has been interpreted as indicative of a large (several AU) inner gap in its disk (Rice et al. 2003), so the absence of CTTS characteristics at $1 \text{ }\mu\text{m}$ in November 2002 might indicate a weakening or halt of accretion through the inner gap. Because GM Aur had no detectable line emission or continuum excess, we treated it as a WTTS and adopted it as a spectral template for veiling. The spectral type for this star in the literature ranges from K3 to K7. It is certainly warmer than K7 in our spectra, with photospheric features similar to stars classified as K2-K3 (CW Tau and UX Tau). We also note that two of other WTTS, TWA 3 (Hen 3-600A) and TWA 14, have been modeled as possessing extremely small disk accretion rates of $\dot{M}_{acc} = 5 \times 10^{-11} M_\odot \text{yr}^{-1}$ on the basis of their H α lines (Muzerolle et al. 2000, 2001b). However, since the derived accretion rates are so small and neither shows significant line or continuum emission in our $1 \text{ }\mu\text{m}$ spectra we have included them with the WTTS and adopted TWA 3 as a veiling template.

The final palette of WTTS spectral templates for determination of veiling and residual emission profiles in the CTTS included only 5 stars, after eliminating V826 Tau and TWA 14. Although 4 of these are identified as K7/MO in the literature, the relative strengths of their Ti, Cr and Si lines led us to sequence them as shown in Figure 1. These correspond to effective spectral types of K2, K7, K7, K7/MO and M3 for veiling determination. With this sequencing our modest number of WTTS templates provided good veiling determinations for the CTTS with the possible exception of the 2 solar type stars, GW Ori and SU Aur. For these stars we assigned SU Aur $r_Y = 0$, since its line depths were comparable to our K2 template after the appropriate rotational broadening, and from there we found that GW Ori, which has a comparable $v \sin i$ to SU Aur, required $r_Y = 0.3$. In addition there were 3 stars with a middle to late K spectral type (CI Tau, HN Tau, and RW Aur A) which appeared to be intermediate between our K2 or K7 templates so we took the unorthodox step of creating a synthetic template from averaging the spectra of these two. It provided an excellent match for the relative line depths of these 3 stars, and we felt the veiling derived with the synthetic template was reliable.

The Y -band veiling, r_Y , for the 38 CTTS with He I $\lambda 10830$ and $P\gamma$ line emission is listed in Table 2. Stars are ordered by veiling, which ranges from $r_Y = 0 - 2$. Veiling is first determined independently in each of the two photospheric orders, and then the average value is adopted and applied to the order with the He I $\lambda 10830$ and $P\gamma$ lines. Subtraction of the veiled standard from this order yields both residual emission line profiles for these two lines and a third assessment of the veiling. We found an excellent agreement for veilings determined from the 3 orders. The error for each veiling measurement is the largest deviation from the adopted value that yields a fit indistinguishable from the best fit, which is typically larger than the dispersion among the orders. When r_Y is less than or equal to 0.5, the veiling error is approximately ± 0.05 . For larger veilings, the error is approximately ± 0.1 . We note that the veiling measurements reported here for the 6 stars that also appear in Edwards et al. (2003) supercede the earlier estimates, which were not evaluated with the same degree of thoroughness.

The process of creating residual profiles results in an improved definition of the emission lines in stars with low veiling, particularly in the line wings. We illustrate this in Figure 2 at $P\gamma$ for two stars with $r_Y = 0.1$, AA Tau and UZ Tau W. Note the effect on the line shape, especially how the wings in the residual profiles are more clearly defined when the photospheric features have been removed.

The residual profiles for $P\gamma$ and He I $\lambda 10830$ for 38 CTTS are presented in Figure 3 and Figure 4, respectively. The 39th CTTS, GM Aur, is excluded since it was not detected in either line. Nine CTTS were observed more than once, and we show the multiple profiles for $P\gamma$ and He I $\lambda 10830$ in Figure 5 and Figure 6, respectively. Most multiple observations are separated by days, except for DG Tau and HL Tau, which are separated by a year. Table 2 presents measurements of the $P\gamma$ and He I $\lambda 10830$ features in the CTTS including kinematic information and emission and absorption equivalent widths. Among the 9 stars with more than one observation, the profiles and their kinematic parameters do not change appreciably with the exception of AA Tau. For these 9 stars, the spectrum included in the *reference sample* is identified with an asterisk, representing one spectrum for each star, and is used for all statistical analyses in figures and text.

In both the figures and Table 2 the spectra are arranged in order of decreasing $1 \mu\text{m}$ veiling. The table separates the stars into groups corresponding to 3 levels of veiling: high ($r_Y \geq 0.5$; 9 stars), medium ($0.3 \leq r_Y < 0.5$; 11 stars) and low ($r_Y \leq 0.2$, 18 stars). The low veiling stars are further divided into 2 subgroups of 9 stars each, according to the width of the $P\gamma$ feature. Average values for kinematic properties of the profiles in each group are identified. Discussion of the profiles and their kinematic properties follows in subsequent sections.

3. ACCRETION DIAGNOSTICS: $P\gamma$ AND $1\ \mu\text{m}$ VEILING

Our NIRSPEC data allows us to evaluate two quantities expected to be sensitive to the disk accretion rate: $P\gamma$ equivalent width and the $1\ \mu\text{m}$ veiling, r_Y . The $P\gamma$ line emission is predicted to arise primarily in magnetospheric accretion columns (Muzerolle et al. 1998a, 2001) and the continuum excess from accretion luminosity, e.g. from accretion shocks at the base of magnetic funnel flows (Calvet & Gullbring 1998). These diagnostics can be used to test magnetospheric accretion models and to establish the extent to which our prime wind diagnostic, He I $\lambda 10830$, is influenced by accretion. We detect $P\gamma$ emission in 38 of the 39 CTTS and $1\ \mu\text{m}$ veiling in 31 of the 39 CTTS. The sole $P\gamma$ non-detection is GM Aur, which as discussed in the previous section appears to be in a quiescent non-accreting state, and we treat it as a WTTS for the remainder of this paper (see Figure 1). In this section we focus on the properties of the $P\gamma$ emission and its relation to veiling. We will discuss the implications of the profile morphology for magnetospheric accretion models in Section 6.1 and examine the spectral energy distribution of the veiling and its relation to disk accretion rate in Section 7. For the intervening sections we simply use r_Y as a quantity likely to be proportional to the instantaneous disk accretion rate.

The $P\gamma$ profiles for 38 CTTS are predominantly in emission; none show blueshifted absorption from a wind while 24% (8 from the reference sample in Figure 3: BM And, DR Tau, DS Tau, GI Tau, RW Aur, RW Aur B, SU Aur, YY Ori plus AA Tau in Figure 5) show redshifted absorption below the continuum, suggesting infall of accreting material in a magnetospheric funnel flow. The $P\gamma$ emission and absorption equivalent widths are listed for each observation in Table 2. The emission equivalent widths range from a high of $18\ \text{\AA}$ (AS353 A) to a low of $0.6\ \text{\AA}$ (CI Tau, V836 Tau) and the absorption equivalent widths from a high of $1.1\ \text{\AA}$ (YY Ori) to a low of $0.2\ \text{\AA}$ (DS Tau and RW Aur A).

We find a remarkably good correspondence between the $P\gamma$ emission equivalent width and r_Y , shown in the top panel of Figure 7. Following standard practise, in the figure the measured equivalent width W_λ is multiplied by the factor $(1 + r_Y)$, which renormalizes it to the photosphere, rather than photosphere plus veiling continuum (Basri & Batalha 1990; Beristain et al. 2001). The figure shows a tight correlation between $P\gamma$ and r_Y for the 31 CTTS with measurable veiling, with a linear correlation coefficient of 0.97 between the logarithm of the veiling and the logarithm of the veiling-corrected $P\gamma$ emission. The figure exaggerates the separation in veiling between the 11 CTTS with the lowest measured veiling, $r_Y \sim 0.1$, and the 7 CTTS non-detections, $r_Y < 0.05$, which were not included in the determination of the correlation coefficient. However all but one of the non detections have $P\gamma$ strengths comparable to those with the lowest veilings so they effectively exhibit the same correlation between $P\gamma$ emission and veiling. The sole exception to the correlation

is TW Hya, which has no detected veiling but robust $P\gamma$ emission comparable to CTTS with $r_Y \sim 0.3$. The tight relation between W_λ ($P\gamma$) and r_Y is reminiscent of, although better defined than, others reported between permitted emission lines and either veiling or disk accretion rates determined from veiling (Basri & Batalha (1990) for $H\alpha$; Muzerolle et al. (1998b) for $H\alpha$ and P_{11} ; Muzerolle et al. (1998c) for $Br\gamma$ and $P\beta$; Doppmann et al. (2003) for $Br\gamma$).

Similarly, the morphology of the $P\gamma$ profiles shown in Figure 3 is reminiscent of $P\beta$ and $Br\gamma$ profiles (Folha & Emerson 2001; Muzerolle et al. 1998c), with broad single peaks sometimes accompanied by redshifted absorption below the continuum. The profiles cover a range of line widths and centroids, which we characterize by measuring 3 kinematic properties: (1) emission centroids which range from $V_c = -150$ to $+29$ km s $^{-1}$; (2) maximum blue wing velocities which range from $V_{bwing} = -400$ to -100 km s $^{-1}$; and (3) line widths measured from the stellar rest velocity to the blueward half-intensity point which range from $V_{BHI} = -250$ to -26 km s $^{-1}$. The latter two focus on emission blueward of the stellar rest velocity in order to avoid complications from redshifted absorption. Measurements of V_{bwing} , V_{BHI} and V_c are plotted against veiling in Figure 8 for all but two stars in the reference sample and listed in Table 2 for all observations. The 2 stars omitted in the figure (CI Tau, UX Tau) have such weak and amorphous $P\gamma$ emission that kinematic features could not be reliably established.

The kinematic data for $P\gamma$ suggest a relation that has not previously been reported: a connection between $P\gamma$ profile morphology and veiling. We illustrate it more directly in Figure 9 where we superpose $P\gamma$ profiles in groups segregated by veiling. The top panel displays profiles for 9 CTTS with high veiling ($r_Y \geq 0.5$), the second panel for 11 CTTS with medium veiling ($0.3 \leq r_Y < 0.5$), and last two panels for 18 CTTS with low or absent veiling ($r_Y \leq 0.2$). The low veiling group is divided into 2 subcategories according to the width of their $P\gamma$ profiles: 9 CTTS in the 3rd panel have narrow $P\gamma$ lines with $V_{BHI} < 60$ km s $^{-1}$ and 9 CTTS in the 4th panel have $P\gamma$ lines in excess of this width.

The trend in profile morphology with veiling is exhibited by the 29 stars in the top 3 panels (i.e. excluding the 9 low veiling stars with broad $P\gamma$ profiles, which will be discussed below). For these 29 stars, $P\gamma$ profiles are normalized to their peak intensities (given for each star in Table 2) to facilitate comparison of profile morphology independent of line strength. Among these 29 stars, the mean linewidth blueward of the stellar velocity V_{BHI} decreases from 135 km s $^{-1}$ to 40 km s $^{-1}$ among the 3 veiling groups, while the mean centroid velocity decreases from $V_c \sim 20$ km s $^{-1}$ to ~ 0 km s $^{-1}$. Remarkably, those in the low veiling subgroup with narrow $P\gamma$ ($V_{BHI} \leq 60$ km s $^{-1}$) all have rather similar profiles after normalization, showing central peaks with an average $V_{BHI} = -40 \pm 10$ km s $^{-1}$, an average $V_c = 2 \pm 8$

km s⁻¹. Most also have a two-component structure suggesting a strong narrow core and a weak broad base. When we compute an average P γ profile for these 9 low veiling stars it is well fit with two gaussians, one a narrow component centered at -2 km s⁻¹ with a FWHM of 52 km s⁻¹ and the other a broad component centered at +6 km s⁻¹ with a FWHM of 176 km s⁻¹.

Although the trend in P γ profile morphology to decrease in width and centroid velocity with decreasing veiling is suggestive it does not include 9 stars with low veiling (24% of the sample). The separation of the low veiling stars into two groups based on P γ line width was effected in order to illustrate the remarkable uniformity for half of the low veiling profiles. The other 9 low veiling stars with broad P γ , superposed in the bottom panel of Figure 9, show an unusual diversity in their morphology. Three (BM And, CI Tau, UX Tau) have broad amorphous emission and low peak intensity (<10% of the continuum flux). Two (BM And and SU Aur) have exceptionally deep and broad redshifted subcontinuum absorption penetrating to 50% of the 1 μ m continuum with emission peaking considerably blueward of the other stars ($V_c < -120$ km s⁻¹). Along with these 4 stars which are completely unlike the rest of the sample, the additional 5 stars in this subgroup (DE Tau, DD Tau, FP Tau, RW Aur B, UZ Tau W) are more typical but are included here because their breadths and blueshifts are larger than those with uniform narrow P γ profiles. (We note that unlike the other superposed profiles in Figure 9, the 9 stars in this subgroup are plotted in residual intensity units, reflecting their true height above the stellar continuum rather than normalized to peak intensity, to avoid mis-representing the amorphous profiles with very low peak intensities.)

In summary, our key findings for P γ and veiling are (1) a robust correlation between emission equivalent width and veiling; (2) a remarkably consistent profile morphology among half of the stars with low veiling showing a two component structure with narrow centered cores and a weak broad base; and (3) a progression in profile morphology with veiling for a sizeable fraction, but not all, of the sample. Systematic variations with veiling of line width and centroid velocity have not, to our knowledge, been previously reported for hydrogen lines in CTTS. We discuss the implication of the veiling dependence of P γ profiles for magnetospheric formation in Section 6.1.

4. WIND DIAGNOSTIC: He I λ 10830

Our NIRSPEC survey probes the innermost wind region in accreting stars with the He I λ 10830 line. The uniqueness of this probe derives from the metastability of its lower level ($2s^3S$), which, although energetically far above (20 eV) the singlet ground state, is

radiatively isolated from it. Whether this metastable level is populated by recombination and cascade or by collisional excitation from the ground state, it will become significantly populated relative to other excited levels owing to its weak de-excitation rate via collisions to singlet states, making it an ideal candidate to form an absorption line. This absorption is essentially a resonant-scattering process since the $\lambda 10830$ transition ($2p^3P^o - 2s^3S$) is the only permitted radiative transition from its upper state to a lower state and the electron density is unlikely to be so high as to cause collisional excitation or de-excitation. This sets up an ideal situation to probe outflowing gas in absorption, provided the conditions are right to excite helium 20 eV above the ground state.

We find He I $\lambda 10830$ features in 38 of the 39 CTTS in our sample; the exception is GM Aur (see Figure 1), suspected to be in a quiescent non-accreting state. Line profiles for each star, ordered by decreasing r_Y , are shown in Figure 4 and additional observations of the 9 stars with multiple observations are in Figure 6. Equivalent widths and kinematic properties are listed in Table 2, sorted by 4 groups corresponding to high, medium and low veiling, with the 18 low veiling objects additionally split two kinematic subgroups based on $P\gamma$ line widths, V_{BHI} .

The predicted sensitivity of He I $\lambda 10830$ to absorption is born out by our observations, where absorption below the $1 \mu\text{m}$ continuum is seen in 34 of the 38 stars (89%). Although blueshifted subcontinuum absorption from outflowing gas is most common (27 of 38 stars, 71%) redshifted subcontinuum absorption from infalling gas is also frequent (18 out of 38 stars, 47%). In 2 stars (5%; GK Tau, UX Tau), the subcontinuum absorption is centered on the stellar rest velocity and is flanked by emission on both sides. Our identification of the presence of blue, red, or centered subcontinuum absorption in each profile is listed in Column 14 of Table 2 by the letters *b*, *r*, *c*. Of the 4 stars with no subcontinuum He I $\lambda 10830$ absorption (CW Tau, RW Aur A, HN Tau, BP Tau) the profiles have asymmetries suggesting either redward or blueward absorption that does not penetrate the $1 \mu\text{m}$ continuum.

Because subcontinuum absorption is often a sizeable contributor to the He I $\lambda 10830$ line, a comparison between emission equivalent width and veiling, which yielded a well defined relationship for $P\gamma$, is not meaningful for He I $\lambda 10830$. While the emission equivalent width above the continuum ranges from $W_\lambda = 0$ to 30.1 \AA , the absorption equivalent width below the continuum in turn ranges from $W_\lambda = 0$ to 10.7 \AA so that a strong helium feature may have a large positive or negative equivalent width, or may have a net equivalent width close to zero. To examine the dependence of the strength of He I $\lambda 10830$ with veiling, we define a *helium activity index* as the sum of the absolute value of the equivalent width of the emission above the continuum (E) and the absorption below the continuum (A). This activity index ($E + A$) ranges from $\sim 1 - 30$ and is plotted against r_Y in the lower panel

of Figure 7. It shows a trend of increasing with veiling, corresponding roughly to that seen for $P\gamma$, although with considerably more scatter. We have separately indicated the helium profiles that are primarily in emission ($E - A/E + A > 0.5$) since the activity index for these stars is dominated by the emission equivalent width, which is directly analogous with the relation found for $P\gamma$. The observed trend relating the helium activity index and veiling indicates that helium excitation is correlated with disk accretion rate.

In order to appreciate the full diversity of helium profiles, we have arranged them into a scheme based on a combination of both veiling level and profile structure. This categorization is shown in Figure 10, where superposed He I $\lambda 10830$ profiles are first grouped by the same 4 categories used for comparing $P\gamma$ profiles in Figure 9 based on veiling and the $P\gamma$ line width (4 horizontal rows), and then further sorted into 3 morphological classes (3 vertical columns). All helium profiles are in the continuum-normalized units of Figure 4, with the exception of TW Hya which was rescaled to half its peak intensity in order to facilitate comparison with the other profiles in its category.

The 3 morphological groups portrayed in Figure 10 are as follows: The left column contains 14 stars with profiles that fall into the general category of “P Cygni-like”, with subcontinuum absorption that is blueward of all or most of the emission and with no redshifted absorption below the continuum. The middle column contains 18 stars with profiles that do have redshifted absorption below the continuum, most of which (13 stars) *also* show subcontinuum blueshifted absorption. The profiles in the right column are from the 6 objects with either central absorption (2 stars), or no subcontinuum absorption (4 stars).

The ensemble of He I $\lambda 10830$ profiles in Figure 10 illustrates that each of the 3 general profile types (blueshifted subcontinuum absorption, both blueshifted and redshifted subcontinuum absorption, and central or no subcontinuum absorption) can be found at all veiling levels. However there is a tendency for broad P Cygni-like profiles to be more common among stars of high veiling (5 out of 9 stars) while narrow emission coupled with both blueshifted and redshifted absorption is more common among stars with low veiling (12 out of 18 stars). Although our time coverage is limited, among the 9 stars with more than one observation we do not see any stars shifting among these profile categories (see Figure 6), suggesting that the profile categories we observe are not primarily due to time variable behavior among the CTTS but are intrinsic to each star.

Examination of the superposed profiles in Figure 10 also shows that the kinematic structure of the subcontinuum blueshifted absorption component is more diverse than that of the red absorption. We discuss the implications of this diversity for wind formation in Section 6.2, and present here a table with basic properties of the blueshifted absorption in Table 3. This includes the equivalent width of the blue absorption below the continuum,

the continuum penetration depth, the full velocity extent of the blue absorption and the corresponding minimum and maximum velocity relative to the stellar rest velocity. At one extreme is an object like DR Tau, where the He I $\lambda 10830$ line is almost entirely in absorption, with a breadth of nearly 500 km s^{-1} , extending from -400 to $+70 \text{ km s}^{-1}$ relative to the star and absorbing 95% of the $1 \mu\text{m}$ continuum over most of that velocity interval. At another extreme, an object like V836 Tau has helium primarily in emission and the narrow blueshifted absorption extends from only -30 to 0 km s^{-1} relative to the star, cutting through the emission feature and penetrating the continuum to a depth of 30%.

In summary, the prevalence in accreting T Tauri stars of blueshifted He I $\lambda 10830$ absorption below the continuum demonstrates the ubiquity of accretion powered winds arising in the immediate vicinity of the star. However the diversity of profile morphologies suggests that the nature of the winds are not identical in all of these accreting stars, a topic we return to in Section 6.2. We also find that He I $\lambda 10830$ is sensitive to infalling gas in magnetospheric accretion flows, discussed further in Section 6.1.

5. CLASS I SOURCES

In addition to the survey of 39 CTTS and 6 WTTS whose accretion properties are well documented from previous studies, we acquired NIRSPEC data for 3 young stellar objects, identified in Table 4, whose spectral energy distributions place them as Class I or borderline Class I/II objects. Two of them, SVS 13 and IRAS 04303+2240, have disk accretion rates comparable to those of the most active Class II CTTS, $\dot{M}_{acc} \sim 10^{-6} M_{\odot} \text{ yr}^{-1}$ and are the driving sources for HH Objects/jets and molecular outflows (references given in Table 4). The third, IRAS 04248+2612, is considerably less active with disk accretion and wind mass loss rates several orders of magnitude smaller, comparable to a typical CTTS (White & Hillenbrand 2004).

The faintness of these embedded sources resulted in lower S/N spectra than for the CTTS, where integration times of 300 seconds for IRAS 04303+2240 and 1200 seconds for SVS 13 and IRAS 04248+2612 yielded S/N of 60, 60, and 20, respectively). For IRAS 04248+2612, the M5.5 photospheric features showed no evidence of veiling. The other two objects have strong emission lines at the location of all the photospheric features, preventing a direct measure of the veiling. For them we estimated the veiling based on the relation between $P\gamma$ and r_Y that we found for the CTTS. If they follow the same relation, their $P\gamma$ equivalent widths indicate $r_Y \sim 1.8$ for IRAS 04303+2240 and $r_Y \sim 0.3$ for SVS 13.

The residual He I $\lambda 10830$ and $P\gamma$ profiles for these 3 stars are shown in Figure 11 and

their line properties are given in Table 5. Overall the profile morphologies for both $P\gamma$ and He I $\lambda 10830$ are similar in character to those found among the CTTS, with the exception of the $P\gamma$ profile of the low accretion rate object IRAS 04248+2612 which has a double rather than single peaked structure. All 3 He I $\lambda 10830$ lines show evidence of winds in the form of blueshifted absorption, penetrating the continuum in SVS 13 and IRAS 04248+2612 but not in IRAS 04303+2240. The He I $\lambda 10830$ profile for SVS 13 is very similar to that of the high accretion rate CTTS DR Tau, in that both are almost entirely in absorption, which is very broad and very deep, extending from the stellar rest velocity to almost 400 km s^{-1} .

6. DISCUSSION OF LINE PROFILES

Our survey of He I $\lambda 10830$ and $P\gamma$ lines in CTTS and 3 Class I sources presents a rich new array of kinematic diagnostics of the star-disk interface region in accreting stars. In this section we discuss how the profile morphology for each of these lines gives insight into magnetospheric accretion flows and accretion powered winds.

6.1. Magnetospheric Contributions to $P\gamma$ and He I $\lambda 10830$

The presence of magnetospheric accretion flows in classical T Tauri stars is inferred from general similarities between observed and model profiles, particularly for hydrogen lines of modest opacity (Muzerolle et al. 2001; Hartmann et al. 1994; Edwards et al. 1994). In the radiative transfer models, line emission arises along the full length of an accretion column characterized by a fairly uniform temperature, connecting the truncated disk to the stellar photosphere. Hydrogen profile characteristics reproduced in the models include broad single peaked emission with a blue asymmetry and the appearance of redshifted inverse P Cygni absorption (IPC) when the optical depth is not too high and the inclination is favorable (i.e. when the line of sight passes through both the infalling gas and the hot accretion shock). In our NIRSPEC data, the presence of redshifted IPC absorption in $P\gamma$ (9/38 CTTS) and He I $\lambda 10830$ (18/38 CTTS) profiles implies that each of these lines probes magnetospheric funnel flows. However, some unexpected profile characteristics pose new challenges to our understanding of the magnetospheric accretion process.

A hydrogen line such as $P\gamma$ is expected to be formed primarily in the accretion flow, and taken in aggregate, our observations appear to support this expectation. The profiles are single peaked with a range of line widths (V_{BHI} from -250 to -26 km s^{-1}), a tendency toward blueward centroids (V_c from -150 to 29 km s^{-1}) and an IPC frequency of 24%. However,

the extremes in linewidths and centroid velocities and their *progression* with veiling are not predicted by existing models.

To quantify the difference between observed and predicted profiles we compare distributions of their kinematic parameters V_{BHI} and V_c in Figure 12. The kinematic parameters for the data are separately plotted for $\text{P}\gamma$ profiles in the high, middle and low veiling groups described in Section 3. Corresponding distributions for the theoretical profiles from magnetospheric accretion models (Muzerolle et al. 2001) are shown in the bottom panel. The theoretical parameters are measured from the online database of $\text{P}\beta$ profiles predicted to arise under a variety of mass accretion rates and disk truncation radii.¹ We selected only those profiles considered by Muzerolle to be appropriate combinations of gas temperature and accretion rate, which are $T = 6000$ or 7000 K at $\dot{M} = 10^{-6} \text{ M}_{\odot} \text{ yr}^{-1}$, $T = 7000$ or 8000 K at $\dot{M} = 10^{-7} \text{ M}_{\odot} \text{ yr}^{-1}$, $T = 8000$ or $10,000$ K at $\dot{M} = 10^{-8} \text{ M}_{\odot} \text{ yr}^{-1}$, or $T = 10,000$ or $12,000$ K at $\dot{M} = 10^{-9} \text{ M}_{\odot} \text{ yr}^{-1}$. Following these constraints, we extracted 128 of the available 272 stark broadened model $\text{P}\beta$ profiles, covering disk truncation radii from ~ 2 to $6 R_*$ seen from 4 viewing angles and evaluated their V_{BHI} and V_c . To facilitate comparison between the theoretical and observed distributions, we rescaled the V_{BHI} and V_c distributions measured from the models to correspond to the appropriate weighting for a random selection of orientation angles.

Although the model and observed profiles span similar ranges of V_{BHI} and V_c for many of the stars, some observed profiles show kinematic properties outside the range of the models. At high veiling 2 of the 9 stars have $V_{\text{BHI}} \sim 50 \text{ km s}^{-1}$ higher than the models. More significantly, at low veiling many stars have $V_{\text{BHI}} < 50 \text{ km s}^{-1}$ and $V_c < 10 \text{ km s}^{-1}$, narrower and more centered than predicted for magnetospheric accretion flows. Moreover, as discussed in Section 3, these narrow and centered $\text{P}\gamma$ kinematic properties (3rd panel of Figure 9) are actually from the narrow component of profiles with a two-component (narrow and broad) structure.

The $\text{P}\gamma$ narrow component is reminiscent of a similar feature in many metallic emission lines in CTTS, usually attributed to formation in a stationary accretion shock at the footpoint of the funnel flow (Batalha et al. 1996; Johns-Krull & Basri 1997; Alencar & Basri 2000; Najita et al. 2000). For example, the FWHM of the narrow component at He I $\lambda 5876$ from the study of BEK, which overlaps significantly with the stars studied here, is $47 \pm 7 \text{ km s}^{-1}$, in comparison to that for the average $\text{P}\gamma$ value of $\sim 52 \text{ km s}^{-1}$. In CTTS metallic lines the proportional contribution of narrow and broad component emission is sensitive to the accretion rate, where the narrow component from the accretion shock dominates over the

¹Available at http://cfa-www.harvard.edu/cfa/youngstars/models/magnetospheric_models.html.

broad component predominantly in stars with low accretion rates.

A comparison of $P\gamma$, He I $\lambda 5876$ (from BEK), and He I $\lambda 10830$ profiles for the 9 stars with low $1\ \mu\text{m}$ veiling and narrow $P\gamma$ lines is shown in Figure 13. (Two were not in the BEK sample, but we include them in the figure for completeness.) Although the He I $\lambda 5876$ lines predate the $1\ \mu\text{m}$ lines by almost a decade, it is apparent that all 3 lines in these stars have relatively narrow emission, and for 7 stars for which we have both $P\gamma$ and He I $\lambda 5876$ the presence of a narrow core near line center is apparent in both lines. In contrast He I $\lambda 10830$ lines are considerably more complex due to the sensitivity of this transition to absorption by infalling and outflowing gas. However, in most cases the velocity extent of the blue or red absorption at He I $\lambda 10830$ appears to be matched by the broad component emission at $P\gamma$ or He I $\lambda 5876$.

If $P\gamma$ narrow component emission, which is only seen in low veiling stars, arises in an accretion shock then the assumption that hydrogen lines in low accretion rate stars primarily trace magnetospheric columns is suspect. A related question is where the accompanying $P\gamma$ broad component is formed. In 3 of the low veiling stars in Figure 13 there is an asymmetric blue wing at $P\gamma$ (AA Tau, GI Tau, TW Hya) with a similar velocity extent to the blue absorption at He I $\lambda 10830$, suggesting it may arise in the wind. A similar inference was reached by Whelan et al. (2004) who found blue wings of hydrogen lines in CTTS to be spatially extended, requiring formation in a wind. The fact that the majority of the CTTS $P\gamma$ profiles show a progression from broad blueshifted emission at high veiling to narrow centered emission cores with broad bases at low veiling could be explained if there is an increasing contribution from wind emission at $P\gamma$ as the veiling increases. Or, if the lines are primarily formed in magnetospheric accretion columns, this behavior needs to be accounted for. In the models it is inclination that is the major influence on line width and asymmetry, while the dominant effect of accretion rate is on line luminosity, although when combined with high temperatures line widths will also be enhanced (Muzerolle et al. 2001). The observed progression with veiling suggests that the paradigm of attributing hydrogen line emission to magnetospheric accretion might need to be readdressed, despite the considerable success of previous comparisons of models and observations.

There is however little doubt that magnetospheric accretion is present in CTTS, attested to by the presence of redshifted IPC absorption in both hydrogen and metallic lines. Yet our data poses challenges for IPC features as well, particularly at He I $\lambda 10830$ where the red absorption is often quite broad (several hundred km s^{-1}) and deep (penetrating up to 50% of the continuum; see section 4 and Figures 4, 6, 10, 13). This kinematic structure suggests that magnetospheric infall does not occur in a simple dipole geometry since the funnel flow has a cross-section perpendicular to the line of sight that narrows toward the

star and becomes much smaller than the projected stellar surface. In the beginning of the funnel flow the speed of the gas also increases along a curved path that is more perpendicular to the line of sight than along it, so it is difficult to have the loci of points having the same line-of-sight velocity component project a large cross-section for a broad velocity range, as required for the observed absorptions. Similar conclusions have also been reached by other authors investigating the geometry of T Tauri magnetospheres via a variety of techniques (Bouvier et al. 2006; Daou et al. 2006; Jardine et al. 2006).

We infer that although magnetospheric accretion along field lines connecting the disk and star is common in CTTS, current models of line formation in these flows, while contributing greatly to our understanding of the star/disk interaction zone, oversimplify the actual situation. Our data suggests that the accretion shock can be a significant contributor to Paschen emission in low accretion rate objects and that a wind may contribute to the blue wings. Whether this calls into question a magnetospheric accretion origin for $P\gamma$ emission in the majority of CTTS is unclear. Although many of the observed $P\gamma$ profiles have kinematic parameters in line with those predicted, the models do not account for the observed progression of $P\gamma$ line widths and centroid velocities with decreasing veiling shown in Figure 9. Thus caution is in order when deriving physical parameters of accretion flows on the sole basis of hydrogen line profiles, since it is clear that even lines of modest optical depth can have multiple sources of origin. In any case, even with multiple emission components contributing to $P\gamma$ emission, each must increase in proportion to the disk accretion rate in order to reproduce the correspondence between line strength and r_Y seen in Figure 7.

6.2. Wind Contributions to He I $\lambda 10830$

The He I $\lambda 10830$ line appears to be a promising means of studying the inner wind, given the high frequency (71%) of CTTS with subcontinuum blueshifted absorption. In comparison, the detection frequency of subcontinuum blueshifted absorption at $H\alpha$, a traditional indicator of inner winds, is only 10% (3 of 31) among CTTS in a sample that closely overlaps the present one (see profiles in BEK). The most striking aspect of blueshifted absorption among CTTS He I $\lambda 10830$ profiles is their considerable diversity – in width, velocity, and penetration depth into the continuum. Blue absorption widths have breadths as wide as 470 km s^{-1} to as narrow as 30 km s^{-1} . The narrow absorption features can have blueshifts as high as 300 km s^{-1} to as low as tens of km s^{-1} . Penetration depths can be as low as 10%, but exceed 50% in 9 stars, and exceed 90% in two stars (DR Tau and TW Hya). This diversity indicates that the innermost winds in accreting stars do not all have the same characteristics, and that a range of wind conditions exist in these stars. However, in all cases the winds

must be accretion powered, since there is no evidence for them in non-accreting WTTS and the He I $\lambda 10830$ line strength, in combined emission plus absorption, is sensitive to the $1\ \mu\text{m}$ veiling. In this section we highlight properties of the He I $\lambda 10830$ blueshifted absorption that speak directly to the wind launch region. We are also undertaking a theoretical examination of profiles formed in winds arising both from the star and the inner disk, using Monte Carlo simulations to explore profiles formed via resonance scattering and in-situ emission (Kwan et al., in preparation). A comparison between observed and theoretical profiles will elaborate on the points made here and demonstrate them more rigorously.

Among the stars with “P Cygni-like” profiles (left column in Figure 10 plus SVS 13 in Figure 11) five have blue absorption which is *both* very broad and very deep (SVS 13, DR Tau, AS 353A, HL Tau, and GW Ori). We argue that these absorption features *require* formation in a wind emerging from the star rather than the disk (see also Edwards et al. 2003). In these cases the combination of the extreme line breadth and depth reveals that all velocities in the wind, from rest to terminal velocity, intercept the $1\ \mu\text{m}$ continuum and scatter a significant fraction of those photons. These geometric constraints are satisfied when the source of the $1\ \mu\text{m}$ continuum is the stellar surface and diverging wind streamlines emerge radially away from the star, thereby absorbing continuum radiation over the full acceleration region of the wind. In contrast, for a disk wind geometry continuum photons from the star will encounter a much narrower range of velocities as they pass through the wind, which will be confined to nearly parallel streamlines emerging at an angle to the disk surface. Even in an x-wind (Shu et al. 1994), where wind streamlines open from a narrow ring in the disk, the full range of velocities in an accelerating wind would not occult the stellar surface. Central to this interpretation is the assumption that the source of the $1\ \mu\text{m}$ continuum photons originates from the stellar surface.

This assumption for the location of the $1\ \mu\text{m}$ continuum appears reasonable, as the continuum likely arises from the photosphere itself or from accretion luminosity on the stellar surface (see Section 7). Even for the largest continuum excesses we observe, $r_Y = 2$, a third of the continuum is contributed by the photosphere. The 5 stars with the most broad and deep blue absorption of the $1\ \mu\text{m}$ continuum, and thus the strongest evidence for winds moving radially away from the star, have r_Y values of 2 (DR Tau), 1.8 (AS 353A), 1 (HL Tau) and 0.3 (SVS 13 and GW Ori), demonstrating that similar absorption features are seen in stars with a range of continuum excesses and photospheric contributions. We refer to this wind geometry as a *stellar wind*, although these winds are clearly deriving their energy from processes related to disk accretion.

The above argument for stellar winds is based on the structure of the blue absorption feature in 5 stars. This interpretation is also consistent with their full helium profiles, which

resemble line formation in a stellar wind under conditions of simple resonance scattering. Such conditions would normally result in classic P Cygni profiles with comparable emission and absorption contributions, as seen for AS353 A, HL Tau, and GW Ori. However, if the accretion disk extends close enough to the star to occult the receding flow and suppress the red emission, then a stellar wind can also account for the full profiles of DR Tau and SVS 13 where He I $\lambda 10830$ is predominantly in absorption. This would result if the stellar wind starts beyond the disk truncation radius, which would be favored, for example, under conditions of high disk accretion rate, resulting in smaller truncation radii (Königl 1991).

For the remaining CTTS interpretation of the He I $\lambda 10830$ profiles is less definitive, although stellar winds are still good candidates for the profiles in the P Cygni group, such as DG Tau, DF Tau, DO Tau, and TW Hya. In these stars the blue absorption is narrow but very blueshifted and emission is the dominant contributor to the profile. Such profiles could be explained if resonance scattering plus an additional source of in-situ emission is present in a stellar wind, where prominent emission would also partially fill in the absorption feature, as observed.

The possibility raised in the previous section, that the wind may contribute to broad component $P\gamma$ emission, gains additional support when $P\gamma$ profiles from stars with high veiling are compared with helium lines. In Figure 14 we present a figure analogous to that of Figure 13 showing $P\gamma$, He I $\lambda 5876$, and He I $\lambda 10830$ profiles, but in this case for 4 stars with large $1\ \mu\text{m}$ veiling and P Cygni-like He I $\lambda 10830$ profiles. In contrast to the narrow emission seen at all 3 lines in the low veiling stars, here most of the lines show broad emission (or in some cases, absorption). Similarly broad, blueshifted emission is seen for both $P\gamma$ and the non-simultaneous He I $\lambda 5876$ lines for 3 of these stars (DR Tau, DG Tau and DL Tau). In BEK we argued that the broad blueshifted component of He I $\lambda 5876$ arose primarily in a wind, which Figure 14 suggests may also be contributing to $P\gamma$ emission. If so, this effect may be an important contributor to the progression of $P\gamma$ profile morphology described in Sections 3 and 6.1. The 4th star, AS 353A, shows a more confusing relation between $P\gamma$ and the non-simultaneous He I $\lambda 5876$ line, where it appears as if the blue side of $P\gamma$ and the red side of He I $\lambda 5876$ may be influenced by absorption.

In addition to the P Cygni profiles with blueshifted absorption likely arising from accretion powered stellar winds, other CTTS He I $\lambda 10830$ profiles have blue absorption that is both narrow and less blueshifted, e.g. DS Tau, UY Aur, V836 Tau. Here disk winds provide a natural explanation for the blue absorption, where stellar photons are intercepted over a narrower range of velocities as they cross parallel wind streamlines emerging from the disk. The magnitude of the blueshift will depend on the relative orientations of the disk and the line of sight, where blueshifts would be smallest for more edge-on systems. There are also

a number of stars where the interpretation of the blueshifted absorption is ambiguous, and on the basis of the He I $\lambda 10830$ profile alone, either a stellar or disk wind might be invoked. There are also 4 CTTS with no subcontinuum blue absorption and 2 with deep, centered absorptions, reminding us that the star-disk interface region is complex and not uniform among all accreting stars.

We consider it likely that both disk and stellar winds are present in most CTTS, but that a combination of factors including inclination, disk geometry, accretion/outflow rates, magnetospheres, and accretion shock properties will all contribute to the formation of an observed profile. If both types of winds are present, then the stellar winds probably emerge predominantly from high latitudes. If so, the signature of stellar winds would be favored in stars seen more pole-on, while disk wind signatures would be favored in stars seen more edge-on. Unfortunately, inclination estimates for most CTTS are not well constrained, and accretion rates are variable, so we have not tried to sort out these effects for our profiles at the present time. Although He I $\lambda 10830$ profile morphologies do not have a one-to-one correspondence with the $1\ \mu\text{m}$ veiling, the fact that good examples of stellar wind signatures are found for stars thought to have high accretion rates and well formed jets (e.g. SVS 13, DR Tau, AS 353A, HL Tau, DG Tau) clarifies that the stellar wind component can be important in stars with significant accretion activity.

7. ORIGIN OF $1\ \mu\text{m}$ VEILING

Continuum emission excesses that veil photospheric features in CTTS spectra are known to come from at least 2 different sources. One is an optical/ultraviolet excess shortward of $0.5\ \mu\text{m}$ that is used to determine disk accretion rates. The spectral energy distribution of the excess emission from 0.32 to $0.52\ \mu\text{m}$ (Valenti, Basri, & Johns 1993; Gullbring et al. 1998) is very well described by theoretical models from accretion shocks formed as magnetically channeled material falls from the disk truncation radius to the stellar surface along magnetospheric field lines (Calvet & Gullbring 1998). In the models the observed continuum emission is attributed to optically thick Paschen continua arising in the heated photosphere (6000 - $8000\ \text{K}$) below the shock plus optically thin emission shortward of the Balmer limit from preshock and postshock gas. There are indications that the emission excess longward of $0.5\ \mu\text{m}$ does not steadily decline with wavelength as expected from the accretion shock models, but this has not been systematically studied since it would require simultaneous observational coverage over a wide wavelength region. However, distributions of veiling among similar ensembles of CTTS indicate that it appears to be relatively constant from $0.5\ \mu\text{m}$ to $0.8\ \mu\text{m}$ (Basri & Batalha 1990; White and Hillenbrand 2004), suggesting that there is

an additional contribution to emission excess. This leads to large uncertainties in bolometric corrections and in corresponding accretion luminosities and mass accretion rates from veilings measured in the red.

A second source of excess continuum emission recognized in accretion disk systems is found at near infrared wavelengths from 2 to 5 μm (Folha & Emerson 1999; Johns-Krull & Valenti 2001). This emission excess is well characterized by a single temperature black body with $T \sim 1400$ K and has been successfully modelled as arising in a raised dusty rim at the dust sublimation radius in the disk (Muzerolle et al. 2003). The amount of the excess is proportional to the accretion luminosity, as the dust is heated by radiation from both the photosphere and the accretion shock. The location of the dust sublimation radius is about 0.07 AU for a K7/M0 star but can be expanded to 0.15 AU when accretion luminosities are high (Eisner et al. 2005).

Our NIRSPEC data provides the first reconnaissance of veiling at 1 μm . This wavelength regime is ideally situated to provide additional insight into the behavior of continuum excess in CTTS since it lies between the regions where 6000-8000 K shocked gas and 1400 K warm dust are dominant contributors. However, this also corresponds to the region where the photospheric emission peaks, which will result in smaller veiling, defined as an excess relative to photospheric flux, for comparable emission fluxes. This is in fact seen, as shown in Figure 15, which compares distributions of r_V , r_Y , and r_K for CTTS, using veilings from the literature for the stars in our NIRSPEC survey. It is seen that maximum values for r_Y are only ~ 2 , compared to maxima of 8 for r_V and 4 for r_K . Similarly 20% of stars with optical excesses do not have measurable veilings at 1 μm . (Veiling values and their references are compiled in Table 6). However, as we show below, the 1 μm veiling on average exceeds that expected from either a 6000-8000 K accretion shock or 1400 K dust, and leads us to confirm that an additional source of excess emission is present in CTTS systems.

The magnitude of the discrepancy is shown in Figure 16, which uses veiling ratios, r_λ/r_Y , to illustrate how, on average, veilings at 1 μm exceed those predicted from either of the two suspected sources of continuum excess emission. The veiling ratios are plotted as a function of T_{eff} in order to account for the differing proportions of photospheric contributions to the measured veiling. We also include predicted veiling ratios that would result either from 8000K accretion shocks (r_B/r_Y and r_V/r_Y) or 1400 K warm dust (r_K/r_Y). Although the CTTS ratios are compiled from non-simultaneous veiling measurements, the ensemble of veiling ratios from many stars consistently shows r_Y to be larger than expected from either accretion shocks or warm dust.

For example, the expected veiling ratio r_K/r_Y is about 20 for warm 1400 K dust around a K7/M0 star. Thus the observed maximum r_K of 4, would only generate a 1 μm veiling

of $r_Y = 0.2$, considerably smaller than the observed maximum of 2. Similarly, the observed distribution of r_K/r_Y ratios indicates that on average r_Y is an order of magnitude larger than would arise from the dust.

The corresponding situation for an 8000 K accretion shock predicts a veiling ratio r_B/r_Y of about 7 for a K7/M0 star. Thus the maximum r_B of 5 would correspond to an r_Y of 0.7 in contrast to the observed maximum of 2. This is consistent among the group of CTTS, where the observed ratios again suggest r_Y is, on average, several times larger than predicted. A similar conclusion can be drawn from the ratio r_V/r_Y , although the average discrepancy here is not as large. This is because by 5700 Å the excess emission is already higher than expected relative to the B-band for an 8000 K accretion shock.

In summary, there is persuasive evidence suggesting that an additional source of continuum emission excess other than 6000-8000 K accretion shocks and 1400 K warm dust is present in accreting T Tauri stars. A simple possibility is that accretion shocks are not uniform in temperature, but include cooler components than modelled to date (White and Hillenbrand 2004). Another is radiation emerging from the region where the rotational energy of the inner disk is dissipated, which would generate lower temperatures than the accretion shocks. Determining the source of this emission and its importance in accreting systems will require simultaneous measurements over a very broad range of wavelengths.

8. CONCLUSIONS

Our key empirical findings from NIRSPEC 1 μ m spectra are:

Veiling at 1 μ m ranges from $r_Y = 0$ to 2 for a sample of 39 CTTS whose veiling at 5700 Å ($r_V = 0.1 - 8$) corresponds to two orders of magnitude in disk accretion rates. Approximately 20% of the CTTS (8/39) showed no detectable continuum excess at 1 μ m ($r_Y < 0.05$). For the 3 Class I sources we observed, 2 have 1 μ m veiling. In the CTTS the 1 μ m veiling is on average larger than expected from recognized sources of continuum excess in accreting stars, either 6000-8000 K accretion shocks on the stellar surface or 1400 K puffed rims at the dust sublimation radius in the disk.

The $P\gamma$ line is in emission in 38/39 CTTS with equivalent widths ranging from 0.6 to 18 Å and in all 3 Class I sources. Profiles have central peaks, none show blueshifted absorption, and 24% of the CTTS show redshifted absorption below the continuum. There is good correlation between $P\gamma$ equivalent width and veiling and the majority of stars also show a relation between $P\gamma$ profile morphology and r_Y , with broader more blueshifted lines at high veiling. Among the 18 stars with $r_Y \leq 0.2$, half show $P\gamma$ profiles with a two component

structure comprised of narrow centered cores ($FWHM \sim 50 \text{ km s}^{-1}$) and a broad base ($FWHM \sim 170 \text{ km s}^{-1}$).

The He I $\lambda 10830$ line, found in 38/39 CTTS and all 3 class I sources, displays a more complex profile morphology. Its resonance scattering properties make it extraordinarily sensitive to outflowing and infalling gas in the vicinity of star, with 89% of the CTTS profiles showing absorption below the continuum. Blueshifted subcontinuum absorption from a wind is found in 71% of the CTTS profiles, redshifted subcontinuum absorption from magnetospheric infall in 47%, and centered subcontinuum absorption in 5%. Blueshifted absorption is found at all veiling levels and displays considerable diversity in its velocity structure, with widths ranging from 30- 470 km s^{-1} and depths penetrating up to 95% of the continuum. Redshifted absorption is more prevalent among stars with low veiling and when present can have widths of several hundred km s^{-1} and penetrate up to 50% of the continuum.

Our key interpretive findings from NIRSPEC 1 μm spectra are:

We attribute the diversity of kinematic structure in He I $\lambda 10830$ subcontinuum blueshifted absorption to the presence of two genres of winds being launched from the star-disk interface region. Some CTTS have profiles requiring a wind moving radially away from the star while others are more readily explained as arising in winds emanating from the inner disk. There are also stars where it is not obvious which genre of wind is dominant. Both winds must be accretion powered since neither is seen in non-accreting WTTS and among the CTTS helium strength correlates with veiling. Stellar wind signatures are found for a range of disk accretion rates, including objects of high accretion rate and well developed jets and HH outflows. We consider it likely that both disk and stellar winds are present in all CTTS, but that a combination of factors, including inclination to the line of sight, disk geometry, accretion/outflow rates, magnetospheres, and accretion shock properties determine which genre of wind is the primary contributor to the He I $\lambda 10830$ profile in a particular star.

The high frequency of redshifted subcontinuum absorption in half of the He I $\lambda 10830$ profiles and a quarter of the $P\gamma$ profiles attests to the presence of magnetospheric accretion flows. However, the breadth and depth of this feature at He I $\lambda 10830$ suggests that complex field topologies rather than simple dipole fields probably link accretion columns from the disk to the star, an idea for which there is growing observational support (Bouvier et al. 2006). Surprisingly, several aspects of $P\gamma$ profile morphology suggest this line may not be solely formed in magnetospheric infall, but may also have important contributions from accretion shocks and winds.

In sum, the combination of He I $\lambda 10830$ and $P\gamma$ lines in the 1 μm region offer rich new

probes of the relation between accretion and outflow in young stars. This paper presents the first empirical overview of these profiles among CTTS and demonstrates the unique power of the He I $\lambda 10830$ line to probe the wind launch region in accreting stars. A companion paper will present theoretical profiles for lines formed via scattering and in-situ emission in winds arising from stars and from disks. The finding that at least some of the highest accretion rate CTTS show signatures for accretion powered stellar winds clarifies that stellar winds must be an important component in accreting systems. This allows for the possibility that magnetized stellar winds rather than magnetospheric disk locking may be the means by which accreting stars spin down to rotational velocities well below break-up (Matt & Pudritz 2005; von Rekowski & Brandenburg 2006; Romanova et al. 2005).

Establishing mass outflow rates from He I $\lambda 10830$ will require good determination of physical conditions in the helium wind, which in turn will require simultaneous spectra of both He I $\lambda 10830$ and He I $\lambda 5876$ to establish the conditions for helium excitation and ionization. Until then the magnitude of the contribution of winds traced by helium, either stellar or inner disk winds, to extended mass outflows and jets and to angular momentum loss from the star or disk remains uncertain.

Acknowledgements: NASA grant NAG5-12996 issued through the Office of Space Science provides support for this project. Thanks to Andrea Dupree for conversations and collaboration in an earlier phase of this work, to Russel White and Catrina Hamilton for IDL scripts and to the queue observers for the Keck-Gemini NIRSPEC program, Tom Geballe and Marianne Takamiya for acquiring the 2001 data, and to an anonymous referee for helpful comments.

REFERENCES

- Ardila, D., Basri, G., Walter, F., Valenti, J., & Johns-Krull, C. 2002, ApJ, 566, 1100
- Alencar, S. H. P., Basri, G., Hartmann, L., & Calvet, N. 2005, A&A, in press
- Alencar, S. H. P. & Basri, G. 2000, AJ, 119, 1881
- Alencar, S. H. P. & Batalha, C. 2002, ApJ, 571, 378
- Basri, G. & Batalha, C. 1990, ApJ, 363, 654
- Batalha, C.C., Stout-Batalha, N.M., Basri, G., & Terra, M.A.O. 1996, ApJS, 103, 211
- Beristain, G., Edwards, S., & Kwan, J. 2001, ApJ, 551, 1037 (BEK)

- Bouvier, J., Alencar, S.H.P., Harries, T.J., Johns-Krull, C.M. & Romanova, M.M. in *Protostars and Planets V*, ed. B. Reipurth, D. Jewitt, & K. Keil (University of Arizona Press)
- Cabrit, S., Edwards, S. Strom, S. E., Strom, K. M. *ApJ*, 354, 687
- Calvet, N. 1997, in *IAU Symp. 182, Herbig-Haro Flows and the Birth of Low Mass Stars*, ed. B. Reipurth & C. Bertout (Dordrecht: Kluwer), 417
- Calvet, N., Hartmann, L., Kenyon, S. J., & Whitney, B. A. 1994, *ApJ*, 434, 330
- Calvet, N. & Gullbring, E. 1998, *ApJ*, 509, 802
- Carr, J. S., Tokunaga, A. T., & Najita, J. 2004, *ApJ*, 603, 213
- Cerqueira, A. H., Velzquez, P. F., Raga, A. C., Vasconcelos, M. J. and de Colle, F. 2006, *A*, 448, 231
- Coffey, D., Bacciotti, F., Woitas, J., Ray, T. P., & Eislöffel, J. 2004, *ApJ*, 604, 758
- Daou, A., Johns-Krull, C., Valenti, J. 2006 *AJ* 131, 520
- Davis, C. J., Ray, T. P., Desroches, L., & Aspin, C. 2001, *MNRAS*, 36, 524
- Doppmann, G. W., Jaffe, D. T., & White, R. J. 2003, *AJ*, 126, 3043
- Dupree, A. K., Brickhouse, N. S., Smith, G. H., & Strader, J. 2005, *ApJ*, 625, L131
- Edwards, S., Fischer, W., Kwan, J., Hillenbrand, L., & Dupree, A. K. 2003, *ApJ*, 599, L41
- Edwards, S., Hartigan, P., Ghandour, L., & Andrulis, C. 1994, *AJ*, 108, 1056
- Ferreira, J. & Casse, F. 2004, *Ap&SS*, 292, 479
- Folha, D. F. M. & Emerson, J. P. 1999, *A&A*, 352, 517
- Folha, D. F. M. & Emerson, J. P. 2001, *A&A*, 365, 90
- Glassgold, A. E., Najita, J., & Igea, J. 2004, *ApJ*, 615, 972
- Goodrich, R. W. 1986, *AJ*, 92, 885
- Guenther, E., & Hessman, F. V. 1993, *A&A*, 276, L25
- Gullbring, E., Calvet, N., Muzerolle, J., & Hartmann, L. 2000, *ApJ*, 544, 927

- Gullbring, E., Hartmann, L., Briceño, C., & Calvet, N. 1998, *ApJ*, 492, 323
- Hartigan, P., Hartmann, L., Kenyon, S., Hewett, R., & Stauffer, J. 1989, *ApJS*, 70, 899
- Hartigan, P., Edwards, S., & Ghandour, L. 1995, *ApJ*, 452, 736 (HEG)
- Hartigan, P. & Kenyon, S. 2003, *ApJ*, 583, 334
- Hartigan, P., Edwards, S., & Pierson, R. 2004, *ApJ*, 609, 261
- Hartmann, L., Hewett, R., & Calvet, N. 1994, *ApJ*, 426, 669
- Herbig, G. H. & Bell, K. R. 1988, *Third Catalog of Emission-Line Stars of the Orion Population* (Lick Obs. Bull. 1111; Santa Cruz: Lick Obs.)
- Herczeg, G. J., Linsky, J. L., Valenti, J. A., Johns-Krull, C. M., & Wood, B. E. 2002, *ApJ*, 572, 310
- Herczeg, G. J. et al. 2005, *AJ*, 129, 2777
- Hinkle, K., Wallace, L., & Livingston, W. C. 1995, *Infrared Atlas of the Arcturus Spectrum, 0.9-5.3 Microns* (San Francisco: ASP)
- Hirose, S., Uchida, Y., Shibata, K., & Matsumoto, R. 1997, *PASJ*, 49, 193
- Hollenbach, D. J., Yorke, H. W., & Johnstone, D. 2000, in *Protostars and Planets IV*, ed. V. Mannings, A. P. Boss, & S. S. Russell (Tucson: Univ. Arizona Press), 401
- Jardine, M., Cameron, A. Collier, Donati, J.-F., Gregory, S. G., Wood, K. 2006 *MNRAS* in press
- Johns-Krull, C.M., & Basri, G. 1997, *ApJ*, 474, 433
- Johns-Krull, C. M. & Valenti, J. A. 2001, *ApJ*, 561, 1060
- Königl, A. 1991, *ApJ*, 370, L39
- Königl, A. & Pudritz, R. 2000, in *Protostars and Planets IV*, ed. V. Mannings, A. P. Boss, & S. S. Russell (Tucson: Univ. Arizona Press), 759
- Kwan, J. & Tademaru, E. 1988, *ApJ*, 332, L41
- Kwan, J. & Tademaru, E. 1995, *ApJ*, 454, 382
- Matt, Sean & Pudritz, R. 2005 *ApJ*, submitted

- McLean, I. S. et al. 1998, *Proc. SPIE*, 3354, 566
- Moriarty-Schieven, G. H., Wannier, P. G., Tamura, M., & Keene, J. 1992, *ApJ*, 400, 260
- Mundt, R., Walter, F. M., Feigelson, E. D., Finkenzeller, U., Herbig, G. H., & Odell, A. P. 1983, *ApJ*, 269, 229
- Muzerolle, J., Calvet, N., Briceño, C., Hartmann, L., & Hillenbrand, L. 2000, *ApJ*, 535, L47
- Muzerolle, J., Calvet, N., & Hartmann, L. 1998a, *ApJ*, 492, 743
- Muzerolle, J., Calvet, N., & Hartmann, L. 2001, *ApJ*, 550, 944
- Muzerolle, J., Hillenbrand, L., Calvet, N., Hartmann, L., & Briceño, C. 2001b, in *ASP Conf. Ser. 244, Young Stars Near Earth: Progress and Prospects*, ed. R. Jayawardhana & T. P. Greene (San Francisco: ASP), 245
- Muzerolle, J., Calvet, N., Hartmann, L., & D'Alessio, P. 2003, *ApJ*, 597, L149
- Muzerolle, J., Hartmann, L., & Calvet, N. 1998b, *AJ*, 116, 455
- Muzerolle, J., Hartmann, L., & Calvet, N. 1998c, *AJ*, 116, 2965
- Najita, J., Edwards, S., Basri, G. & Carr, J. 2000, in *Protostars and Planets IV* ed Mannings, V. Boss, A. and Russell, S.S., (Tucson, U. of Arizona Press) p. 457
- Najita, J., Carr, J. S., & Mathieu, R. D. 2003, *ApJ*, 589, 931
- Reid, N. 2003, *MNRAS*, 342, 837
- Reipurth, B. & Bally, J. 2001, *ARA&A*, 39, 403
- Rice, W. K. M., Wood, K., Armitage, P. J., Whitney, B. A., & Bjorkman, J. E. 2003, *MNRAS*, 342, 79
- Richer, J. S., Shepherd, D. S., Cabrit, S., Bachiller, R., Churchwell, E. *Protostars and Planets IV* (Tucson: University of Arizona Press; eds Mannings, V., Boss, A.P., Russell, S. S.), p. 867
- Romanova, M.M., Ustyugova, G.V., Koldoba, A.V., Lovelace, R.V.E 2005, *ApJ* 635, L165
- von Rekowski, B. & Brandenburg, A. 2006, *Astronomische Nachrichten*, 327, 53
- Shu, F., Najita, J., Ostriker, E., Wilkin, F., Ruden, S., & Lizano, S. 1994, *ApJ*, 429, 781

- Solf, J. 1994, in ASP Conf. Ser. 57, *Stellar and Circumstellar Astrophysics*, ed. G. Wallerstein & A. Noriega-Crespo (San Francisco: ASP), 22
- Strom, S. E., Vrba, F. J., & Strom, K. M. 1976, *AJ*, 81, 314
- Takami, M., Chrysostomou, A., Bailey, J., Gledhill, T. M., Tamura, M., & Terada, H. 2002, *ApJ*, 568, L53
- Terebey, S., Shu, F. H., & Cassen, P. 1984, *ApJ*, 286, 529
- Valenti, J. A., Basri, G., & Johns, C. M. 1993, *AJ*, 106, 2024
- Whelan, E. T., Ray, T. P., Davis, C. J. 2004, *A&A*, 417, 247
- White, R. J. & Hillenbrand, L. A. 2004, *ApJ*, 616, 998

Table 1. T Tauri Sample

Object (1)	Sp Type (2)	HJD (3)	r_V (4)	$\log \dot{M}_{\text{acc}}$ (5)	Ref (6)	$\log \dot{M}_{\text{wind}}$ (7)	Ref (8)	$\dot{M}_{\text{wind}}/\dot{M}_{\text{acc}}$ (9)
CTTS								
AA Tau ..	M0	605.0,606.9*	0.15-0.63	-8.5	1	-9.1	2	0.25
AS 353 A.	K5	605.7,606.7*	5.10	-5.4	2	-7.6	2	6.3×10^{-3}
BM And ..	K5	604.8	...	>-9*	3
BP Tau ...	K7	605.9	0.41-0.63	-7.5	1	(-9.7)	2	(6.3×10^{-3})
CI Tau ...	K7	605.9	0.39-0.54	-6.8	2	-8.9	2	7.9×10^{-3}
CW Tau ..	K3	604.8,607.0*	1.70	-6.0	2	-7.1	2	7.9×10^{-2}
CY Tau ..	K7	606.8	1.20	-8.1	1	-10.0	2	1.3×10^{-2}
DD Tau ..	M4	604.9	2.90	-6.3	2	-8.5	2	6.3×10^{-3}
DE Tau ..	M1.5	606.0	0.57	-7.6	1	-9.2	2	2.5×10^{-2}
DF Tau ...	M2	605.0	0.52-1.60	-6.8	1	-8.3	2	3.2×10^{-2}
DG Tau ..	K5	235.9*,605.8	2.00-3.60	-5.7	2	-6.5	2	0.16
DK Tau ..	K7	604.9,606.9*	0.49	-7.4	1	-8.5	2	7.9×10^{-2}
DL Tau ...	M0	605.0	1.10-2.40	-6.7	2	-8.9	2	6.3×10^{-3}
DN Tau ..	K7	606.0	0.08	-8.5	1	-9.4	2	0.13
DO Tau ..	M0	604.8	4.70	-6.8	1	-7.5	2	0.20
DQ Tau ..	K7	606.0	0.17-0.18	-9.2	1	-8.7	2	3.2
DR Tau ..	K7	605.0*,606.0,606.9	6.40-10.0	-5.1	2	-8.6	2	3.1×10^{-4}
DS Tau ...	K2	605.9	0.96	-7.9	1	(-9.3)	2	(4.0×10^{-2})
FP Tau ...	M5	605.0	0.08-0.18	-7.7	2	(-10.7)	2	(1.0×10^{-3})
GG Tau ..	M0	605.0	0.14-0.50	-7.8	1	-9.1	2	5.0×10^{-2}
GI Tau ...	M0	606.0	0.24	-8.0	1	-9.4	2	4.0×10^{-2}
GK Tau ..	K7	606.0	0.23	-8.2	1	-9.2	2	0.10
GM Aur ..	K7	605.1	0.21-0.22	-8.0	1	(-10.0)	2	(1.0×10^{-2})
GW Ori ..	G5	606.1	...	-6.4	4
HK Tau ..	K7	606.1	1.10	-6.5	2	-8.8	2	5.0×10^{-3}
HL Tau ...	K7-M2	235.9,605.8*	...	-5.4	5	-6.8	6	4.0×10^{-2}
HN Tau ..	K7	604.8	0.76	-8.9	1	-8.1	2	6.3
LkCa 8 ...	M0	604.9	0.05-0.24	-9.1	1	-9.6	2	0.32
RW Aur A	K1	605.1	1.70-2.00	-5.8	2	-7.6	2	1.6×10^{-2}
RW Aur B	K3	605.1	...	-7.3	6	-8.0	6	0.20
SU Aur ...	G2	607.0	...	-8.0	4
TW Hya ..	K7	605.2*,606.1	...	-9.3	7
UX Tau ..	K2	607.0

Table 1—Continued

Object (1)	Sp Type (2)	HJD (3)	r_V (4)	$\log \dot{M}_{\text{acc}}$ (5)	Ref (6)	$\log \dot{M}_{\text{wind}}$ (7)	Ref (8)	$\dot{M}_{\text{wind}}/\dot{M}_{\text{acc}}$ (9)
UY Aur . .	M0	605.0,607.0*	0.20-1.30	-7.2	1	-8.2	2	0.10
UZ Tau E	M1.5	605.9	0.73	-5.7	2	-7.6	2	1.3×10^{-2}
UZ Tau W	M3	605.9	...	-8.0	8
V836 Tau.	K7	606.0	0.00-0.06	-8.2	2	(-10.1)	2	(1.3×10^{-2})
XZ Tau...	M3	605.8	...	-8.1	9
YY Ori...	K7	607.1	1.80	-5.5	2	(-9.6)	2	(7.9×10^{-5})
WTTS								
LkCa 4...	K7	607.0	0.0	...	2
TWA 3...	M3	606.1	...	-10.3	7
TWA 14..	M0	606.2	...	-10.3	10
V819 Tau.	K7	235.9	0.0	...	2
V826 Tau.	K7	604.9	0.0	...	2
V827 Tau.	K7	606.0	0.0	...	2

Note. — Col 2: Spectral types from HEG, Herbig & Bell (1988), Reid (2003); Col 3: Heliocentric Julian Date (2,452,000 +); for multiple observations an asterisk indicates membership in the reference sample; Col 4: Veiling at 5700 Å from HEG; Col 5: mass accretion rate in $M_{\odot} \text{ yr}^{-1}$; Col 7: mass loss rate in $M_{\odot} \text{ yr}^{-1}$; parentheses indicate an upper limit; Col 9: Ratio of the mass loss rate to the mass accretion rate

References. — (1) Gullbring et al. 1998; (2) HEG; (3) Guenther & Hessman 1993; (4) Gullbring et al. 2000; (5) Calvet et al. 1994; (6) White & Hillenbrand 2004; (7) Muzerolle et al. 2000; (8) Hartigan & Kenyon 2003; (9) Valenti et al. 1993; (10) Muzerolle et al. 2001b.

Table 2. CTTS Veilings and Profiles

Object	r_Y	P_γ							He I $\lambda 10830$				
		V_{bwing} (km s $^{-1}$)	V_{BHI} (km s $^{-1}$)	V_c (km s $^{-1}$)	Peak Intensity	Em W_λ (Å)	Ab W_λ (Å)	Ab Type	V_{bwing} (km s $^{-1}$)	V_{rwing} (km s $^{-1}$)	Em W_λ (Å)	Ab W_λ (Å)	Ab Type
(1)	(2)	(3)	(4)	(5)	(6)	(7)	(8)	(9)	(10)	(11)	(12)	(13)	(14)
CTTS: High 1 μm Veiling													
DR Tau ..	2.0*	-400	-122	-25	1.64	12.6	0.4	r	-400	400	1.6	10.7	b
	2.0	-400	-111	-21	1.80	12.3	0.4	r	-450	400	1.2	11.4	b
	2.0	-350	-108	-17	1.93	13.7	0.3	r	-450	400	0.1	12.5	b,r
AS 353 A .	2.0	-400	-108	18	1.54	17.7	-300	500	4.8	2.2	b
	1.8*	-350	-90	29	1.40	14.6	-400	500	5.4	2.8	b
CW Tau ..	1.0	-400	-167	-46	0.96	10.2	-450	450	14.0
	1.3*	-350	-82	-23	1.71	11.8	-400	400	16.4
DL Tau...	1.1	-350	-149	-18	1.41	14.5	-500	450	21.4	0.4	b
HL Tau...	1.0	-250	-144	-15	0.89	9.5	-200	350	2.5	4.0	b
	1.0*	-300	-122	-2	1.19	10.4	-400	400	4.5	3.8	b
DG Tau ..	0.9*	-350	-141	-20	0.93	8.7	-500	350	8.7	1.2	b
	0.7	-300	-138	-25	0.77	6.6	-350	350	6.8	0.1	b
RW Aur A	0.9	-400	-186	-52	1.20	11.9	0.2	r	-350	300	15.0
DK Tau ..	0.5*	-350	-124	-35	0.49	3.4	-500	400	0.2	5.8	b,r
	0.5	-350	-83	4	0.35	2.7	-500	400	...	6.7	b,r
HN Tau ..	0.5	-400	-201	-23	0.69	9.6	-500	500	30.1
Mean ^a ...	1.1 (0.5)	-360 (30)	-135 (40)	-19 (22)	1.18 (0.41)	10.9 (3.4)	0.1 (0.1)	...	-440 (60)	410 (70)	11.5 (10.0)	2.8 (3.6)	...
CTTS: Medium 1 μm Veiling													
DS Tau...	0.4	-400	-130	-42	0.58	4.2	0.2	r	-500	400	2.0	1.4	b,r
HK Tau ..	0.4	-350	-128	-39	0.32	2.7	-450	300	1.1	1.0	b,r
UY Aur ..	0.4	-350	-105	-26	0.60	4.2	-300	300	4.5	0.4	r
	0.4*	-350	-59	-7	0.57	3.3	-300	300	3.6	0.8	b,r
YY Ori...	0.4	-350	-122	-48	0.60	3.6	1.1	r	-350	450	1.4	3.6	b,r
BP Tau...	0.3	-350	-94	-19	0.58	3.6	-250	250	5.8
DF Tau ..	0.3	-300	-76	-12	0.71	4.2	-200	300	3.6	1.3	b
DO Tau ..	0.3	-300	-64	-9	1.35	7.8	-200	300	2.4	2.5	b

Table 2—Continued

Object (1)	r_Y (2)	P_γ							He I $\lambda 10830$				
		V_{bwing} (km s $^{-1}$)	V_{BHI} (km s $^{-1}$)	V_c (km s $^{-1}$)	Peak Intensity	Em W_λ (Å)	Ab W_λ (Å)	Ab Type	V_{bwing} (km s $^{-1}$)	V_{rwing} (km s $^{-1}$)	Em W_λ (Å)	Ab W_λ (Å)	Ab Type
(1)	(2)	(3)	(4)	(5)	(6)	(7)	(8)	(9)	(10)	(11)	(12)	(13)	(14)
GG Tau ..	0.3	-300	-126	-18	0.40	3.3	-350	450	5.1	0.2	b
GK Tau ..	0.3	-300	-109	-4	0.24	1.8	-300	350	2.1	2.8	c
GW Ori ..	0.3	-400	-115	-2	0.50	4.7	-450	400	5.0	4.4	b
UZ Tau E	0.3	-250	-157	-51	0.47	4.0	-300	300	3.4	0.2	r
Mean ^a ...	0.3 (0.1)	-330 (50)	-110 (30)	-23 (19)	0.57 (0.29)	3.9 (1.5)	0.1 (0.3)	...	-330 (100)	350 (70)	3.2 (1.6)	1.7 (1.5)	...
CTTS: Low 1 μm Veiling, Narrow P_γ													
AA Tau ..	0.2	-350	-94	-46	0.29	1.5	0.5	r	-400	400	4.4	0.6	r
	0.1*	-300	-37	23	0.16	0.9	-400	400	1.9	2.0	r
CY Tau ..	0.1	-350	-47	-6	0.42	2.0	-250	250	2.4	2.5	b,r
GI Tau ...	0.1	-350	-45	-1	0.53	3.2	0.3	r	-350	400	2.2	3.7	b,r
LkCa 8 ...	0.05	-300	-34	-4	0.16	1.0	-250	350	1.7	1.5	r
DN Tau ..	0.0	-400	-28	4	0.24	1.1	-350	350	2.1	1.7	b,r
DQ Tau ..	0.0	-200	-42	0	0.20	0.8	-450	350	9.4	0.3	b
TW Hya...	0.0*	-350	-58	0	1.71	8.8	-350	350	13.6	5.3	b
	0.0	-250	-54	2	1.64	8.6	-350	250	18.1	4.0	b
V836 Tau.	0.0	-100	-26	3	0.22	0.6	-150	350	1.7	2.2	b,r
XZ Tau...	0.0	-300	-44	1	0.21	1.0	-325	250	2.8	1.2	b
Mean ^a ...	0.0 (0.0)	-290 (90)	-40 (10)	2 (8)	0.42 (0.50)	2.2 (2.6)	0.0 (0.1)	...	-320 (90)	340 (50)	4.2 (4.2)	2.3 (1.5)	...
CTTS: Low 1 μm Veiling, Broad P_γ													
CI Tau ...	0.2	0.06	0.6	-200	350	0.1	2.2	b,r
DE Tau ..	0.2	-250	-128	-12	0.28	2.4	-350	350	1.9	0.7	b
BM And..	0.1	-350	-250	-150	0.09	0.8	0.9	r	-300	300	2.6	2.6	r
DD Tau ..	0.1	-300	-106	-49	0.38	2.2	-150	250	0.5	0.2	b
FP Tau...	0.1	-300	-153	-90	0.16	1.0	-300	200	0.5	1.2	b,r
RW Aur B	0.1	-150	-85	-9	0.14	0.7	0.5	r	-300	400	1.5	2.8	r
UZ Tau W	0.1	-300	-91	-44	0.25	1.4	-250	250	0.3	0.8	b,r
SU Aur ...	0.0	-400	-199	-120	0.17	1.4	0.6	r	-450	200	0.1	2.1	b,r

Table 2—Continued

Object (1)	r_Y (2)	P_γ							He I $\lambda 10830$				
		V_{bwing} (km s ⁻¹)	V_{BHI} (km s ⁻¹)	V_c (km s ⁻¹)	Peak Intensity	Em W_λ (Å)	Ab W_λ (Å)	Ab Type	V_{bwing} (km s ⁻¹)	V_{rwing} (km s ⁻¹)	Em W_λ (Å)	Ab W_λ (Å)	Ab Type
		(3)	(4)	(5)	(6)	(7)	(8)	(9)	(10)	(11)	(12)	(13)	(14)
UX Tau	0.0	0.09	1.3	-400	300	2.3	2.0	c
Mean ^a	0.1 (0.1)	-280 (80)	-130 (40)	-54 (44)	0.18 (0.11)	1.3 (0.6)	0.2 (0.3)	...	-300 (90)	290 (70)	1.1 (1.0)	1.6 (0.9)	...

Note. — Col 2: An asterisk following r_Y identifies the observation chosen for the reference sample. Col 6: Peak emission intensity in units of the continuum. Col 8,13: equivalent width of all absorption below the continuum. Col. 9,14: Type of absorption (b) blue; (c) central; (r) red

^aMean profile parameters for the reference sample from each veiling group; standard deviation in parentheses.

Table 3. Blue He I $\lambda 10830$ Absorption in 27 CTTS

Object (1)	W_λ (\AA) (2)	% Abs. (3)	ΔV (km s^{-1}) (4)	V_{\min} (km s^{-1}) (5)	V_{\max} (km s^{-1}) (6)
AS 353 A.	2.8	60	220	-80	-300
CI Tau ...	1.2	43	140	-60	-200
CY Tau ..	1.5	68	130	-70	-200
DD Tau ..	0.2	15	160 ^a	-10	-170
DE Tau ..	0.7	16	190	-140	-330
DF Tau ..	1.3	49	150	-50	-200
DG Tau ..	1.2	33	200	-250	-450
DK Tau ..	3.7	80	410	-40	-450
DL Tau...	0.4	28	60	-100	-160
DN Tau ..	0.3	13	120	-210	-330
DO Tau ..	2.5	69	160	-40	-200
DQ Tau ..	0.3	13	90	-160	-250
DR Tau ..	10.7	95	470	70	-400
DS Tau...	0.3	23	60	-80	-140
FP Tau...	0.8	31	120	30 ^b	-90
GG Tau ..	0.2	15	60	-150	-210
GI Tau ...	0.6	15	180	-140	-320
GW Ori ..	4.4	73	380 ^a	-60	-440
HK Tau ..	0.5	13	270	-150	-420
HL Tau...	3.8	55	380	-20	-400
SU Aur...	0.6	20	330 ^a	-90	-420
TW Hya..	5.3	98	230	-100	-330
UY Aur ..	0.4	45	60	-90	-150
UZ Tau W	0.3	10	190	-60	-250
V836 Tau.	0.2	51	30	0	-30
XZ Tau...	1.2	46	220	-100	-320
YY Ori...	0.9	40	110	0 ^b	-110

Note. — Col 3: Percentage of continuum absorbed at the deepest point of the profile; Col 4: Range of velocities for blue absorption; Col 5: Minimum velocity of blue absorption; Col 6: Maximum velocity of blue absorption.

^aTwo distinct blueshifted absorption components.

^bBlueshifted absorption component is blended with a redshifted absorption component; V_{\min} is the local maximum in the blended region.

Table 4. Class I Objects

Object (1)	Sp Type (2)	Ref (3)	HJD (4)	$\log \dot{M}_{\text{acc}}$ (5)	$\log \dot{M}_{\text{wind}}$ (6)	Ref (7)	$\dot{M}_{\text{wind}}/\dot{M}_{\text{acc}}$ (8)
SVS 13	K:	1	605.8,606.8	-5.2 ^a	-6.2	3	0.10 ^a
04248+2612	M5.5	2	606.9	-9.0	-9.1	2	0.79
04303+2240	M0.5	2	605.9	-6.1	-6.8	2	0.20

Note. — Col 4: Heliocentric Julian Date (2,452,000 +); Col 5: mass accretion rate in $M_{\odot} \text{ yr}^{-1}$; Col 6: mass loss rate in $M_{\odot} \text{ yr}^{-1}$; Col 8: Ratio of mass loss rate to mass accretion rate.

^aaccretion rate assumed to be 10 times the mass-loss rate.

References. — (1) Goodrich 1986; (2) White & Hillenbrand 2004; (3) Davis et al. 2001.

Table 5. Class I Veiling and Profiles

Object	r_Y	$P\gamma$							He I $\lambda 10830$				
		V_{bwing} (km s $^{-1}$)	V_{BHI} (km s $^{-1}$)	V_c (km s $^{-1}$)	Peak Intensity ^a	Em W_λ (Å)	Ab W_λ (Å)	Ab Type ^b	V_{bwing} (km s $^{-1}$)	V_{rwing} (km s $^{-1}$)	Em W_λ (Å)	Ab W_λ (Å)	Ab Type ^b
SVS 13	0.4	-200	-79	15	0.77	5.4	-350	100	...	4.7	b
	0.3	-200	-58	25	0.69	4.2	-350	100	...	4.4	b
04248+2612	0.0	-200	-45	-4	0.41	1.7	-350	200	3.5	0.7	b
04303+2240	1.8	-350	-111	-11	2.08	15.4	-350	300	12.3

^aPeak emission intensity in units of the continuum.

^bClassification of absorption components: (b) blue.

Table 6. CTTS Mean B, V, Y, K Veiling

Object	r_B	r_V	r_Y	r_K	r_B/r_Y	r_V/r_Y	r_K/r_Y
AA Tau ..	0.27	0.31	0.15	0.38	1.80	2.07	2.53
AS 353 A.	3.45	5.10	1.90	...	1.82	2.68	...
BM And..	0.10	1.40	14.00
BP Tau...	0.80	0.71	0.30	0.72	2.67	2.37	2.40
CI Tau...	...	0.47	0.20	2.35	...
CW Tau..	...	1.25	1.15	1.09	...
CY Tau ..	0.82	1.20	0.10	...	8.20	12.00	...
DD Tau	2.90	0.10	29.00	...
DE Tau ..	0.88	0.57	0.20	1.05	4.40	2.85	5.25
DF Tau ..	1.25	0.93	0.30	0.81	4.17	3.10	2.70
DG Tau ..	2.70	3.15	0.80	1.43	3.38	3.94	1.79
DK Tau ..	0.69	0.49	0.50	1.62	1.38	0.98	3.24
DL Tau...	2.64	1.64	1.10	...	2.40	1.49	...
DN Tau ..	0.16	0.07	0.00	0.21	6.40	2.80	8.40
DO Tau	4.70	0.30	1.90	...	15.67	6.33
DQ Tau	0.18	0.00	0.30	...	7.20	12.00
DR Tau ..	4.30	8.14	2.00	4.00	2.15	4.07	2.00
DS Tau...	1.00	0.83	0.40	1.10	2.50	2.07	2.75
FP Tau...	...	0.14	0.10	0.40	...	1.40	4.00
GG Tau ..	0.90	0.30	0.30	0.26	3.00	1.00	0.87
GI Tau...	0.60	0.24	0.10	0.72	6.00	2.40	7.20
GK Tau ..	0.11	0.17	0.30	1.11	0.37	0.57	3.70
GM Aur ..	0.19	0.22	0.00	0.30	7.60	8.80	12.00
GW Ori ..	0.00	...	0.30	...	0.00
HK Tau	1.10	0.40	2.75	...
HL Tau...	1.00
HN Tau ..	0.60	0.76	0.50	...	1.20	1.52	...
LkCa 8...	0.15	0.15	0.05	...	3.00	3.00	...
RW Aur A	3.20	2.04	0.90	...	3.56	2.27	...
RW Aur B	0.10
SU Aur...	0.00	0.60	24.00
TW Hya..	...	0.29	0.00	0.09	...	11.60	3.60
UX Tau	0.00
UY Aur ..	0.75	0.53	0.40	1.65	1.88	1.32	4.12
UZ Tau E	...	0.73	0.30	2.43	...
UZ Tau W	0.10
V836 Tau.	...	0.04	0.00	1.60	...
XZ Tau...	0.00
YY Ori...	...	1.80	0.40	4.50	...

Note. — 1. Veilings are means from the following compilations: r_B : Basri & Batalha (1990), Gullbring et al. (1998); r_V : Alencar & Batalha (2002), HEG, Muzerolle et al. (1998b); r_Y : this paper; r_K : Folha & Emerson (1999), Johns-Krull & Valenti (2001), Muzerolle et al. (2003) 2. In calculating ratios, objects with r_Y non detections are set to $r_Y = 0.025$.

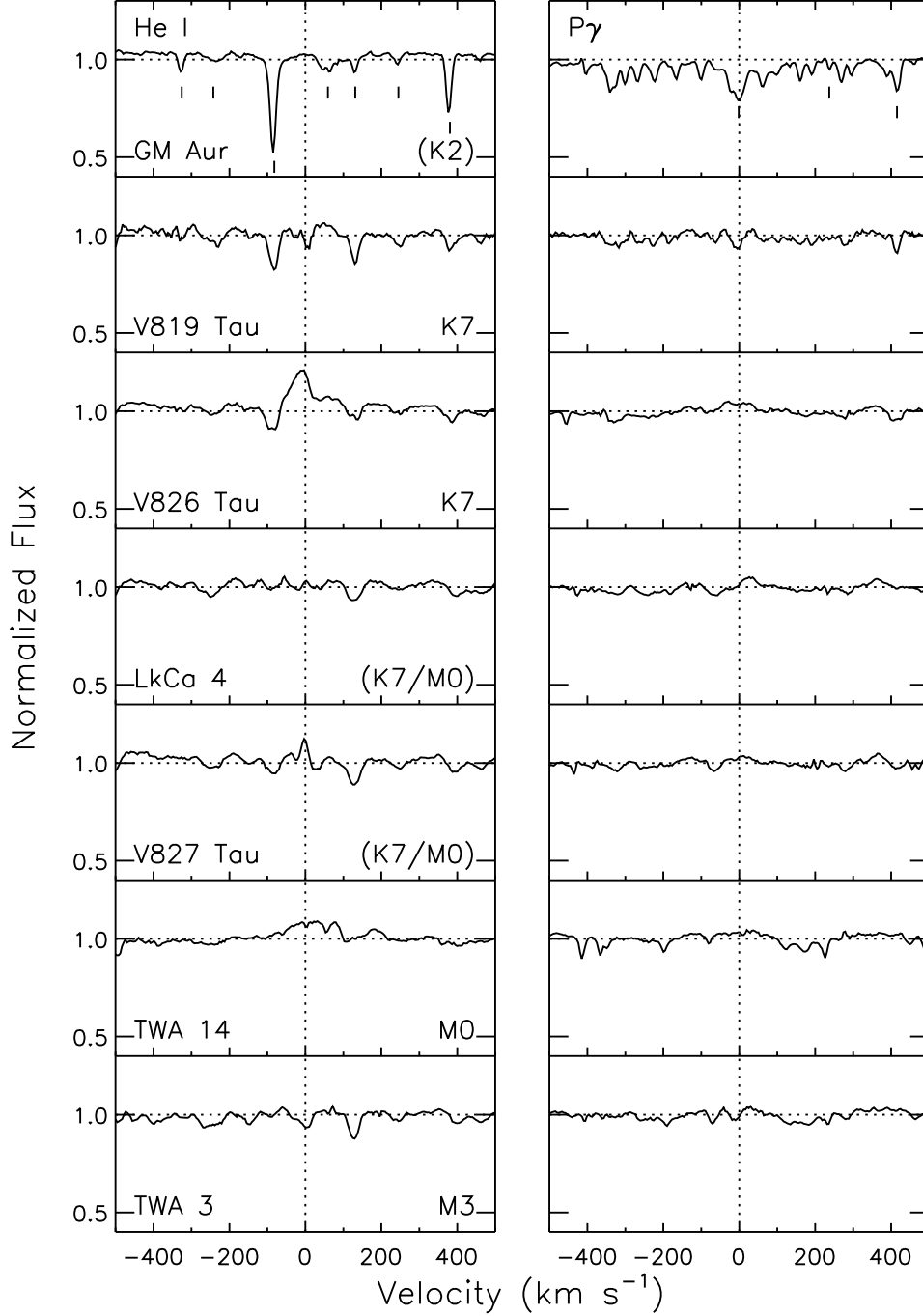


Fig. 1.— Spectral regions of He I $\lambda 10830$ and $P\gamma$ for 6 WTTS plus GM Aur (see Table 1). Photospheric features marked with vertical lines are identified in the text, except for the numerous features from CN 0-0 near $P\gamma$. Ordering is by *apparent* spectral type, given in parentheses when it differs from published values. Fluxes are normalized to the continuum, velocities measured relative to the stellar photosphere, and spectra are unbinned (i.e. at the instrumental resolution.)

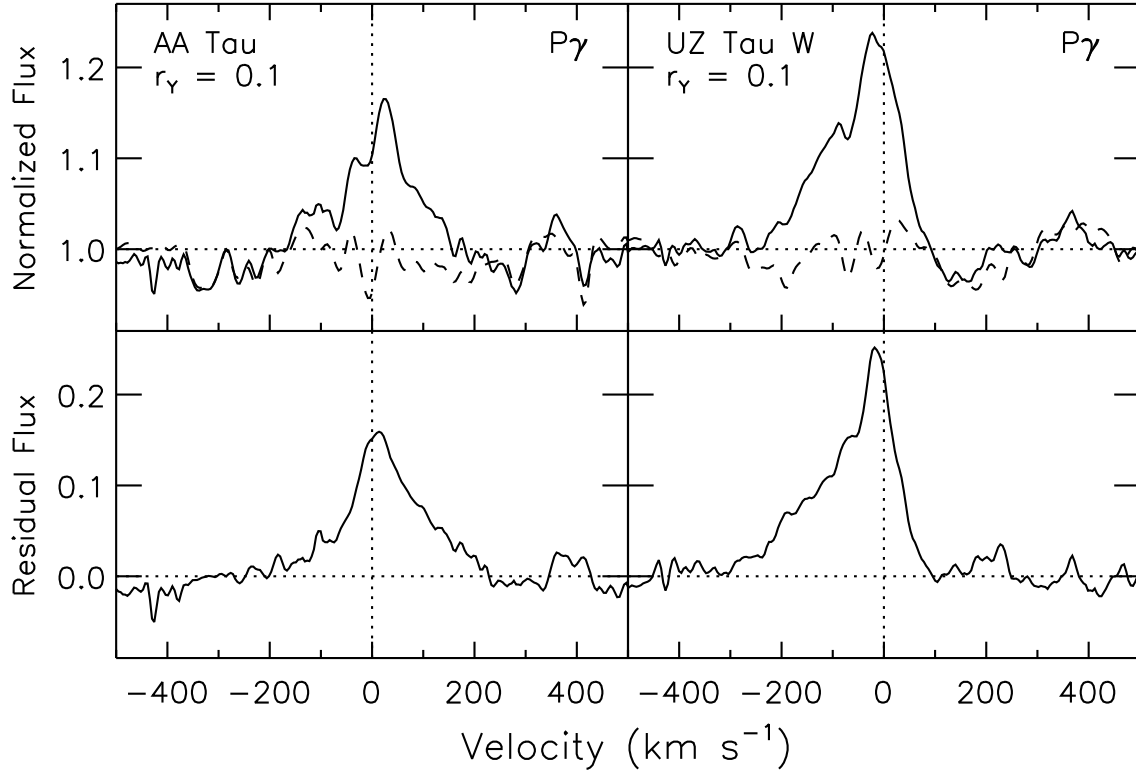


Fig. 2.— Demonstration of *residual profile* determination at $P\gamma$ in AA Tau and UZ Tau W. The top row shows fluxes relative to the continuum for the CTTS (solid line) and for the veiled template (dashed line). The resultant residual profiles after subtraction of the template from the star are shown in the lower row. Templates are V819 Tau (K7) for AA Tau and TWA 3(M3) for UZ Tau W. Velocities are relative to the stellar photosphere.

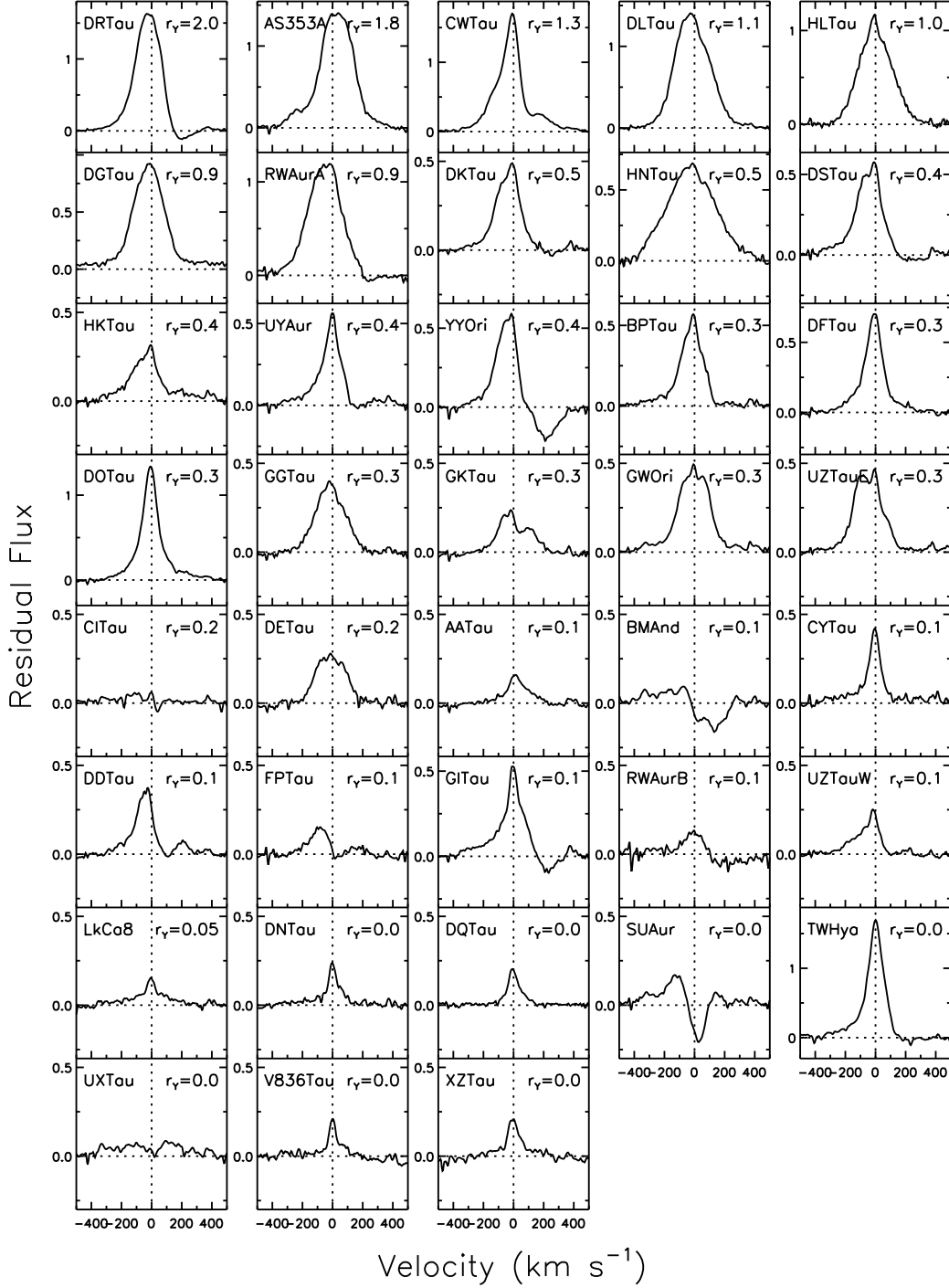


Fig. 3.— *Residual* $P\gamma$ profiles from the reference sample for 38 CTTS (listed in Table 1), ordered by decreasing $1\ \mu\text{m}$ veiling r_γ . Velocities are relative to the stellar photosphere and spectra are plotted with 3 pixel binning.

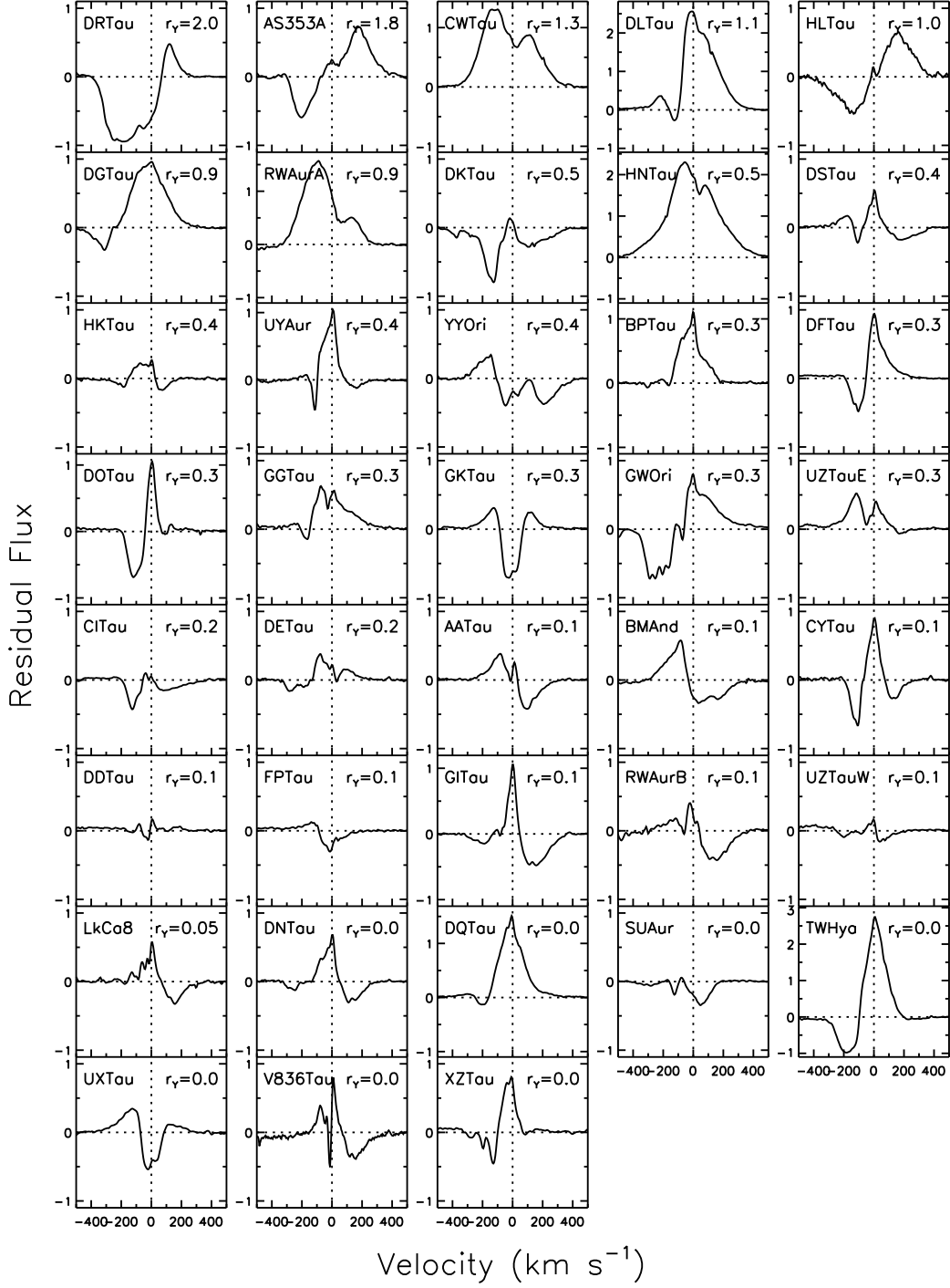


Fig. 4.— *Residual* He I $\lambda 10830$ profiles from the reference sample for 38 CTTS ordered by decreasing $1 \mu\text{m}$ veiling r_Y . Velocities are relative to the stellar photosphere and spectra are plotted with 3 pixel binning.

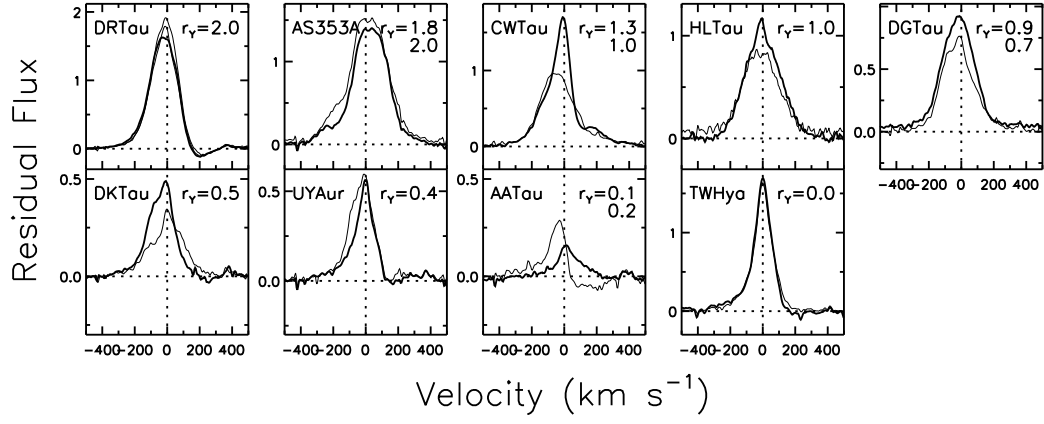


Fig. 5.— Multiple observations of $P\gamma$ residual profiles for 9 CTTS. For each object, the spectrum from the reference sample is denoted by a heavier line.

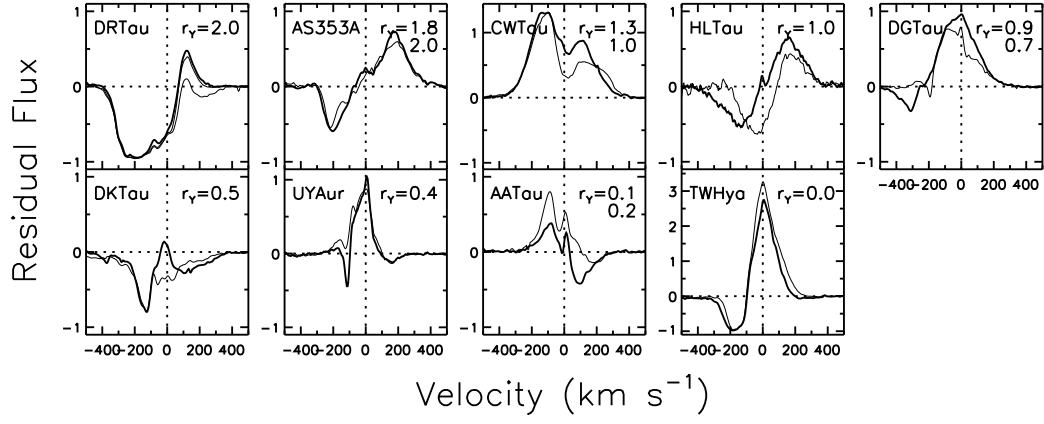


Fig. 6.— Multiple observations of He I $\lambda 10830$ residual profiles for 9 CTTS. For each object, the spectrum from the reference sample is denoted by a heavier line.

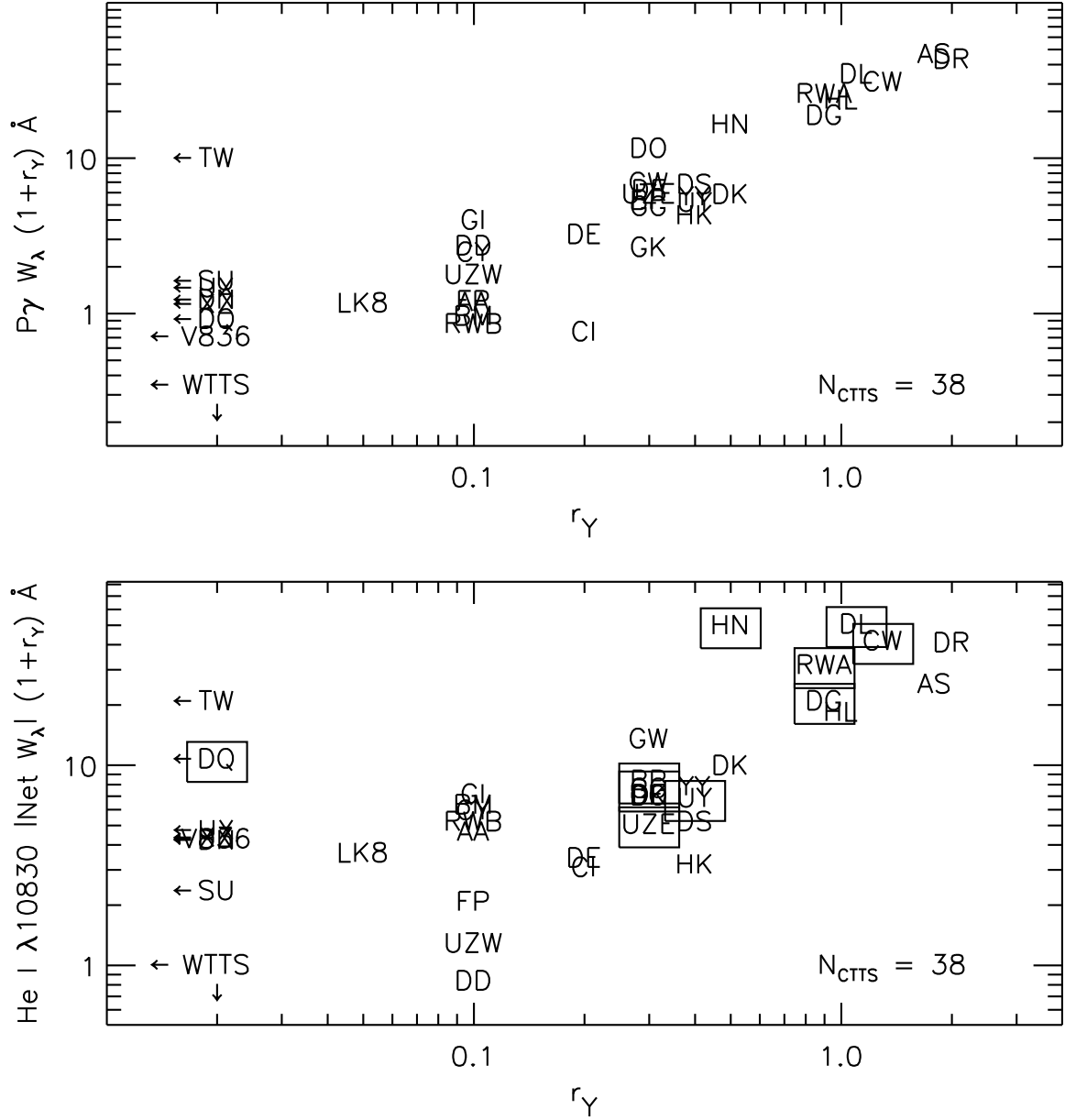


Fig. 7.— *Top panel:* Veiling-corrected $P\gamma$ emission equivalent width versus Y-band veiling for 38 CTTS from the reference sample. *Bottom panel:* Veiling corrected He I $\lambda 10830$ activity index (sum of absolute values of emission plus absorption equivalent widths) versus Y-band veiling for the same stars. In the He I $\lambda 10830$ panel a box around the name of the star indicates its equivalent width is primarily in emission (see text). Veiling non-detections are shown at $r_Y = 0.02$ for clarity. The location of the 6 WTTS plus GM Aur are also indicated.

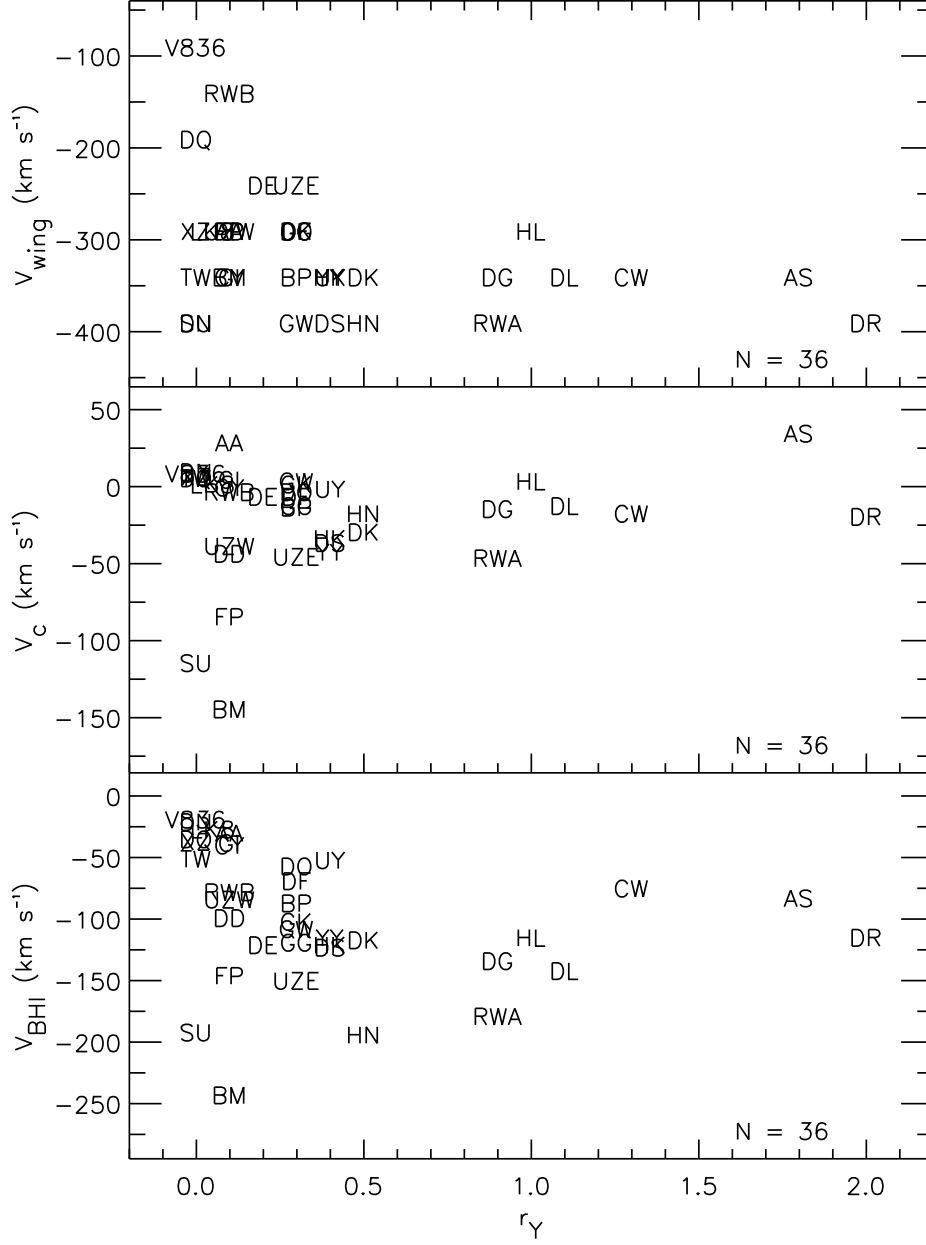


Fig. 8.— Kinematic parameters V_{wing} , V_{BHI} , and V_c for $P\gamma$ profiles plotted against veiling.

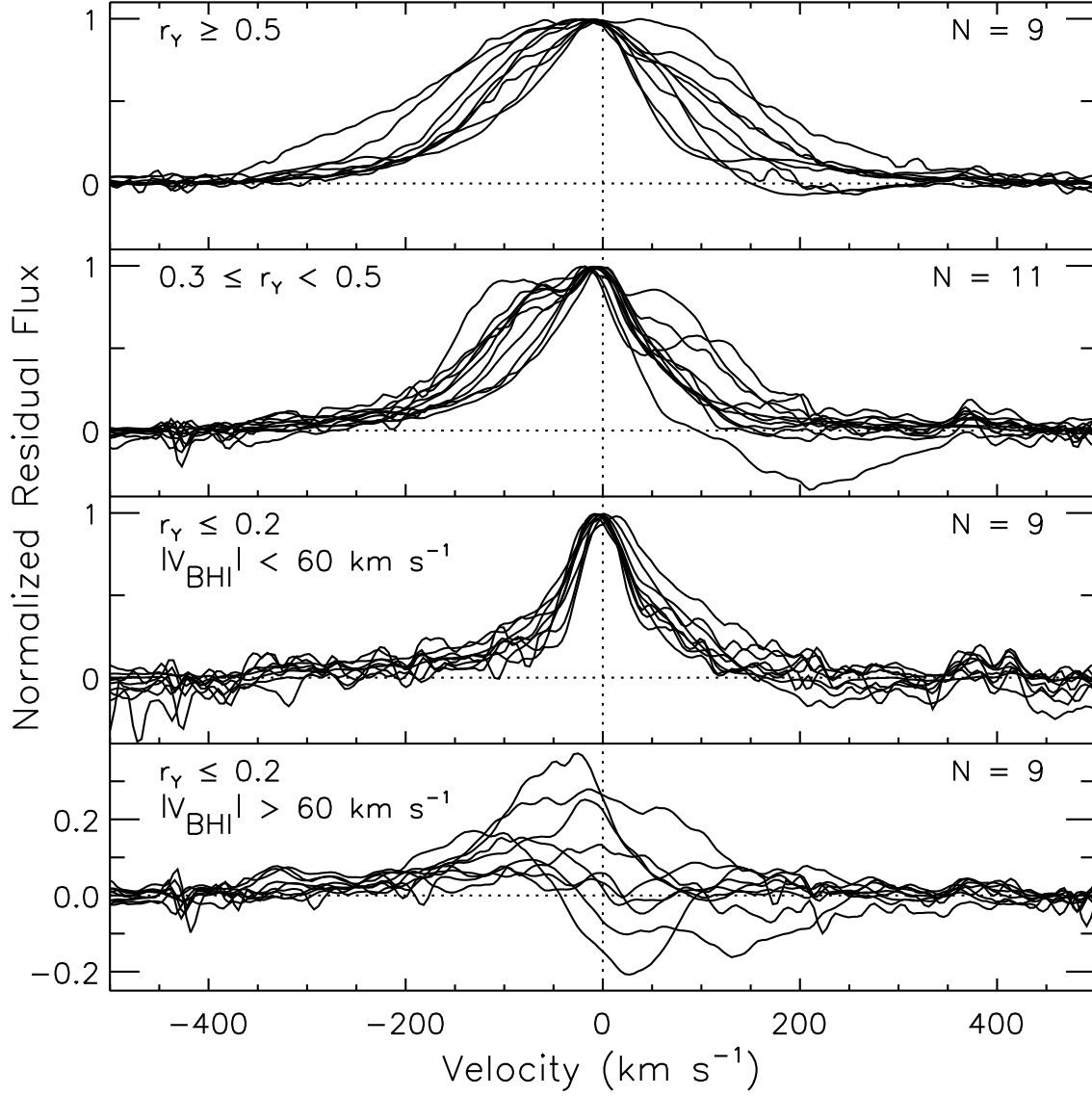


Fig. 9.— Superposed P γ residual profiles from the reference sample grouped by veiling, with the lowest veiling group subdivided into narrow and wide profiles (panels 3 and 4). In the top 3 panels profiles are normalized to their peak intensities. In the lower panel the residual profiles are not normalized in order not to distort the very weak amorphous emission characterizing 3 stars.

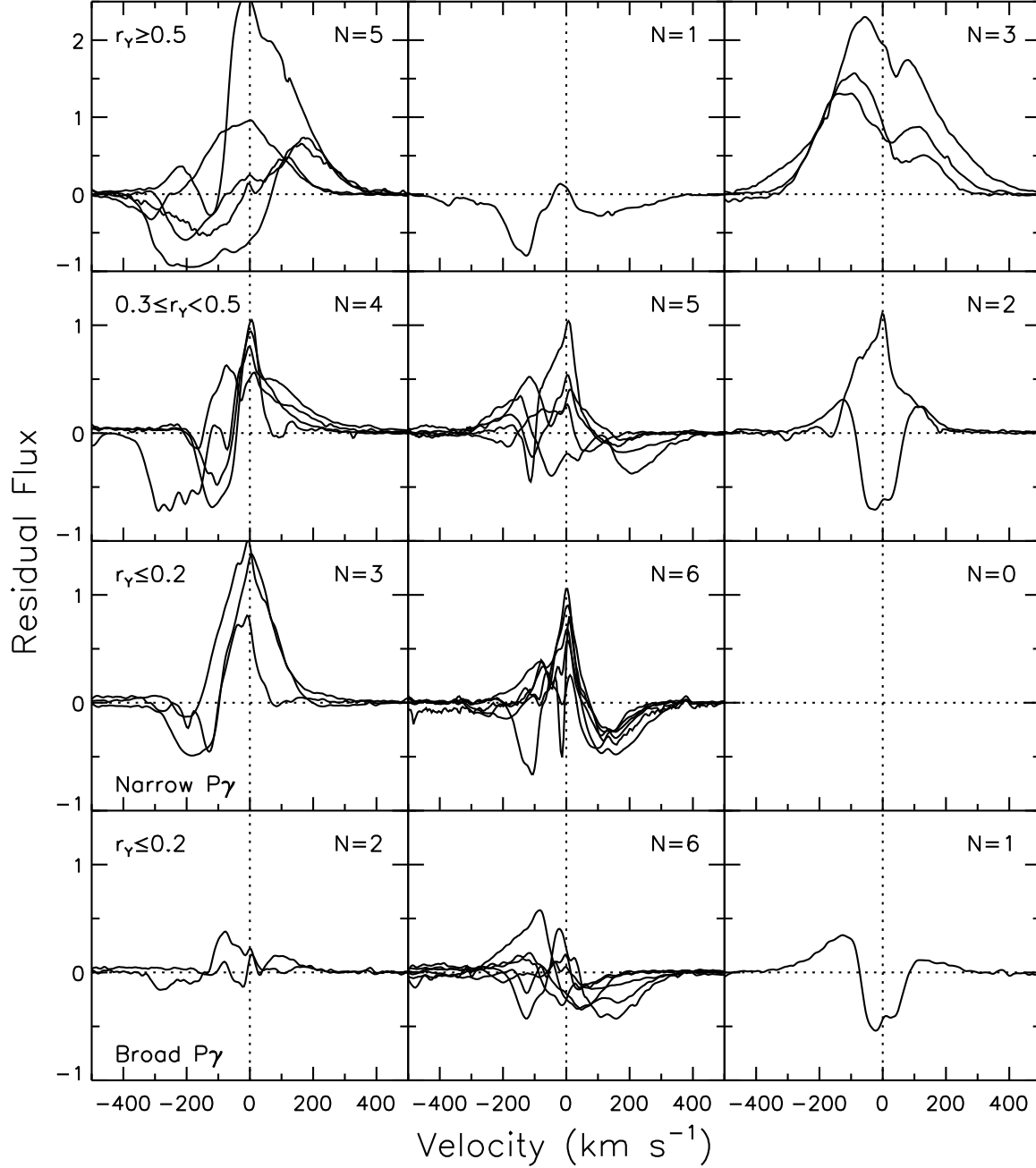


Fig. 10.— Superposed He I $\lambda 10830$ residual profiles grouped by $1 \mu\text{m}$ veiling (horizontal rows) and general morphology (vertical columns). Veiling groups are identical to figure 9, with the low veiling group subdivided by the width of P γ . Morphology groups are: *left*: “P-Cygni like”, *middle*: red absorption below the continuum and *right*: other.

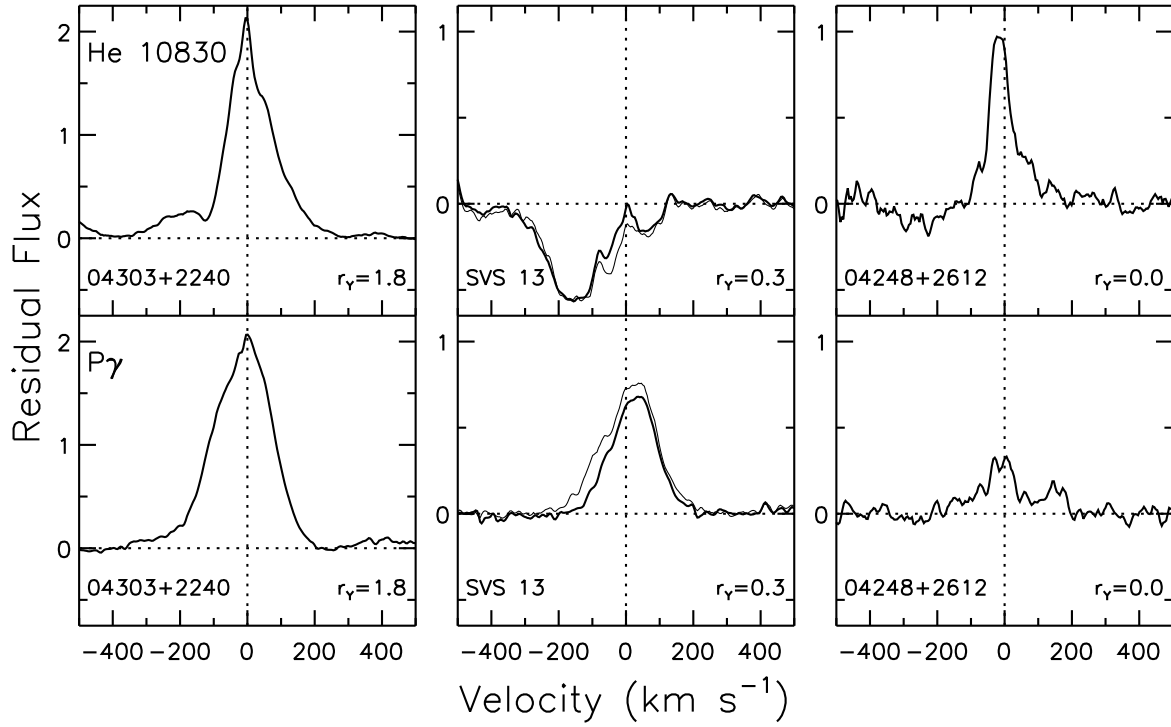


Fig. 11.— Residual He I $\lambda 10830$ and P γ profiles for the Class I sources in order of decreasing $1 \mu\text{m}$ veiling r_Y . The 2 spectra for SVS 13 were taken a day apart; the reference spectrum ($r_Y = 0.3$) is shown with a heavier line than the other ($r_Y = 0.4$). No photospheric features were seen for SVS 13 or 04303+2240 and these profiles are referenced relative to the velocity of ambient molecular material.

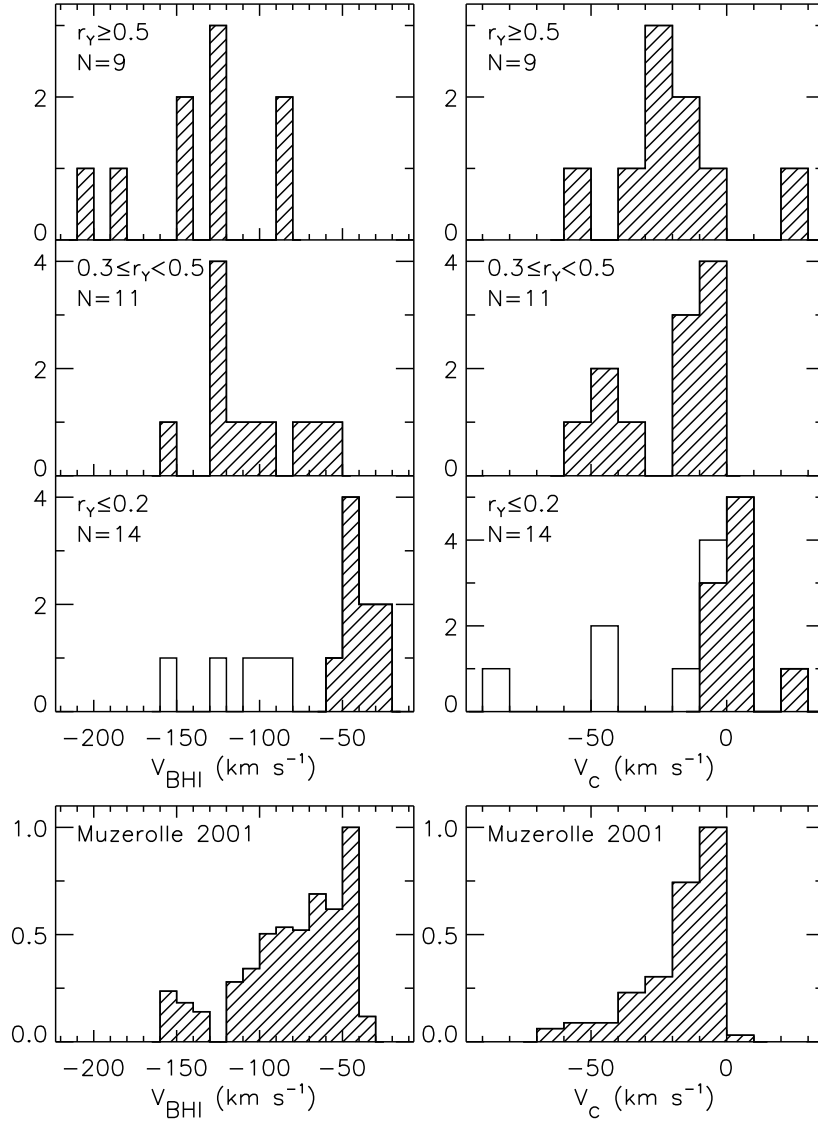


Fig. 12.— Comparison of histograms of kinematic parameters V_{BHI} (left column) and V_c (right column) for observed and theoretical Paschen line profiles. Observed values from $P\gamma$ are separately shown in the first 3 rows for high, middle and low $1\mu\text{m}$ veiling. Theoretical values from online model $P\beta$ profiles (Muzerolle et al. 2001) are in the bottom row. The distribution for the low veiling group excludes 4 stars with $P\gamma$ profiles that bear no resemblance to the models (BM And, SU Aur, CI Tau, UX Tau), making comparisons meaningless. We have separately hatched the remaining 5 stars in the low veiling group with broad $P\gamma$ profiles to emphasize the trend toward decreasing line width and centroid velocity with veiling. The model histogram is normalized to unity and weighted for a random distribution of viewing angles.

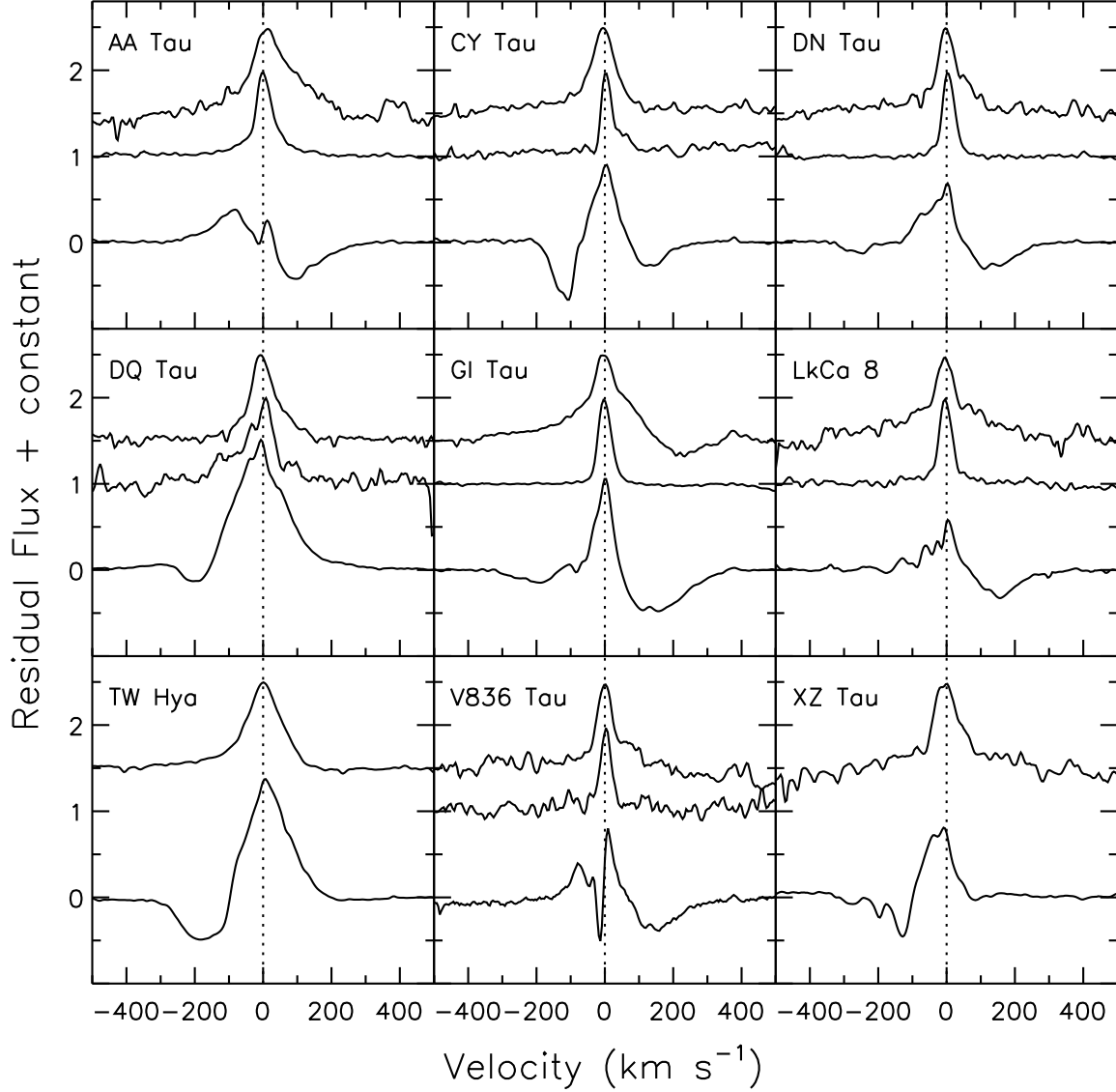


Fig. 13.— Comparison of $P\gamma$ (top), He I $\lambda 5876$ (middle, from BEK), and He I $\lambda 10830$ (lower) profiles for 9 CTTS with low veiling and narrow $P\gamma$ lines. $P\gamma$ and He I $\lambda 5876$ are normalized to their peak intensities to facilitate comparison of their kinematic structure. The He I $\lambda 10830$ profiles are in residual intensity units, except for TW Hya which has been rescaled to half its actual peak intensity. No He I $\lambda 5876$ spectra are available for TW Hya or XZ Tau.

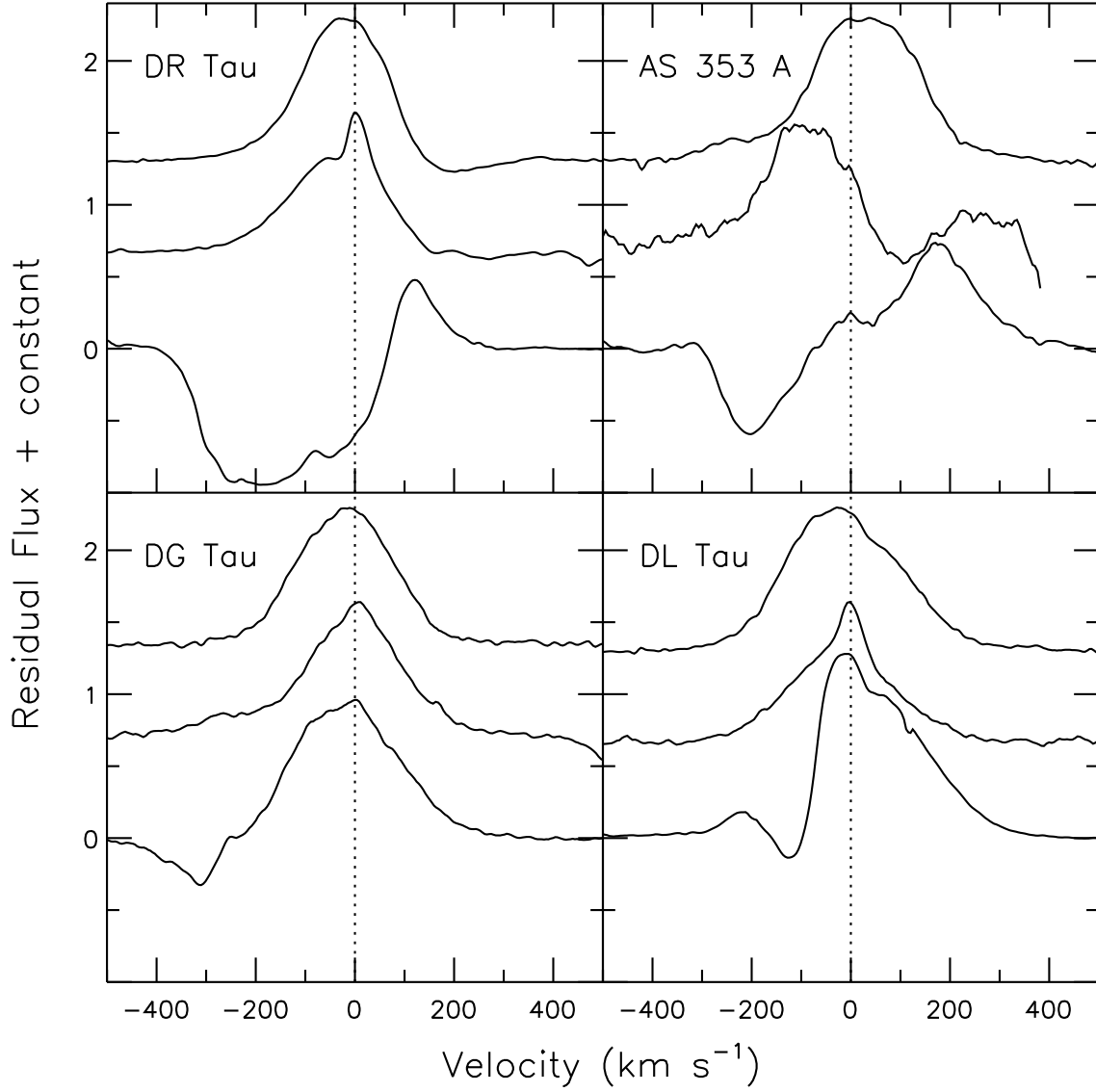


Fig. 14.— Comparison of P γ (top), He I λ 5876 (middle, from BEK), and He I λ 10830 (lower) profiles for 4 CTTS with high veiling and broad P γ lines. P γ and He I λ 5876 are normalized to their peak intensities to facilitate comparison of their kinematic structure. The He I λ 10830 profiles are in residual intensity units.

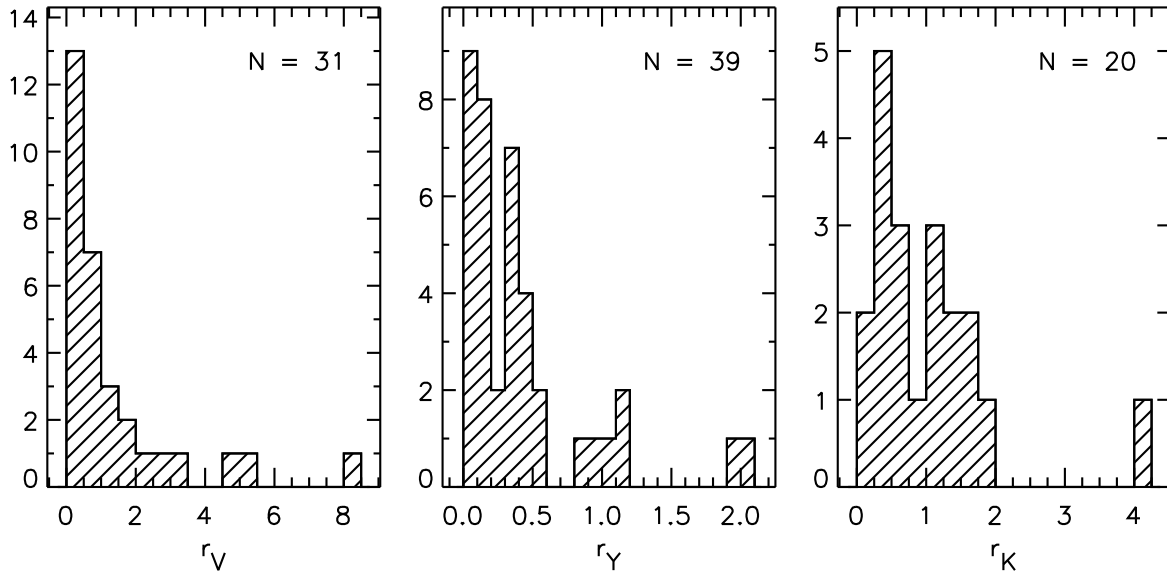


Fig. 15.— Comparison of veiling distributions at V, Y and K. Only stars from the current survey are included, but the non-simultaneous data for V and K from the literature does not include all the stars in our survey.

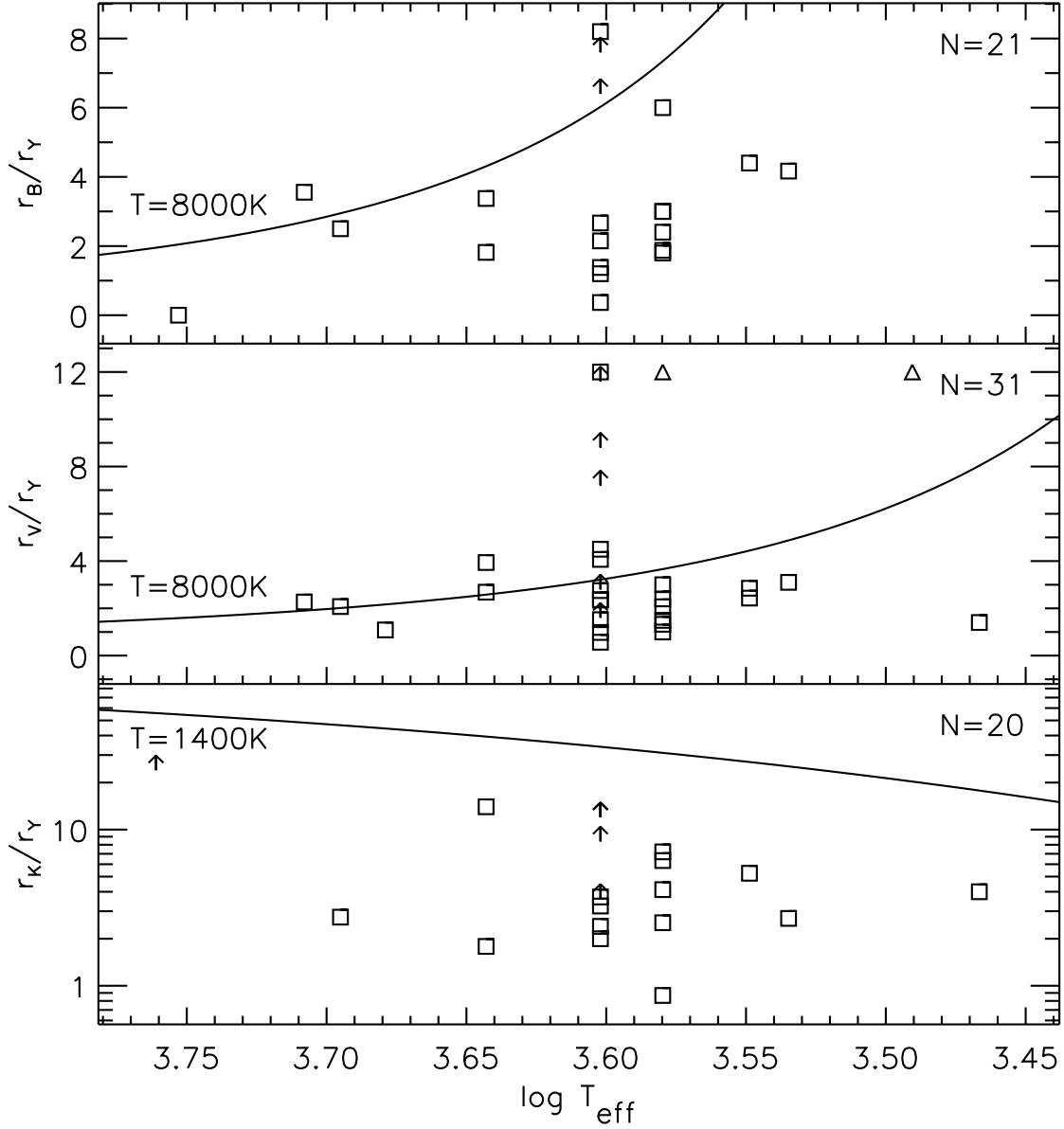


Fig. 16.— Ratios of B , V , and K band veiling to Y band veiling plotted as a function of effective temperature. Stars with measured veilings at each pair of wavelengths are plotted as open squares using mean values given in Table 6. Two stars in the r_V/r_Y plot have ratios too high to fit in the figure (15.7 for DO Tau and 29.0 for DD Tau) and are shown with triangles. To include objects with non-detections at r_Y , we set r_Y to an upper limit of $r_Y = 0.025$. These are shown as open arrows, representing lower limits on the ratio. The solid line shows the predicted ratio for a photospheric T_{eff} with an excess blackbody source of 8000 K (top two panels) or 1400 K (bottom panel). Note that the ratios are scaled linearly in the first two panels and logarithmically in the lower one.